Green Chemistry

TUTORIAL REVIEW

View Article Online
View Journal | View Issue

Cite this: *Green Chem.*, 2025, **27**, 10071

Advances and future perspectives of composite strategies in vanadium-/manganese-based cathode materials for aqueous zinc-ion batteries

Tao Song,[a] Weifeng Fan,[a] Yu Hu,[a] Heng Zhang *[b] and Youcun Bai*[b]

Received 7th April 2025,
Accepted 11th July 2025

DOI: 10.1039/d5gc01694k

rsc.li/greenchem

Aqueous zinc-ion batteries (AZIBs) have attracted much attention in recent years as an emerging and promising energy storage technology with low cost and high safety. Among the various cathode materials, vanadium-based compounds and manganese-based materials have been widely studied due to their rich resources, diverse structures and abundant valence states. However, the application of vanadium-based/manganese-based compounds is limited due to their easy structural collapse and dissolution, low conductivity, side reactions and unclear energy storage mechanism. Recent studies have found that the combination of vanadium-based/manganese-based materials and other (including carbon and non-carbon) materials is an effective strategy to solve the above problems. In this review, the research and development of vanadium-based/manganese-based composite materials in recent years are reviewed, including green synthesis strategies for composite support materials such as carbon nanotubes (CNTs), graphene (GO), metal–organic framework (MOF)–derived carbon, MXenes and other compound carriers. Moreover, the analysis of their synthesis methods and their advantages in reducing the use of toxic reagents are thoroughly discussed. Additionally, the zinc storage mechanisms of these composites are systematically elaborated. Finally, the future development direction of AZIBs is proposed, which is expected to stimulate more innovative research to promote the development and practical application of AZIBs.

Green foundation

1. Eco-friendly synthesis methods that effectively reduce hazardous waste and energy consumption are presented. Additionally, there has been progress in reducing the use of harmful electrolytes through the use of water-based alternatives, which enhances the safety and sustainability of batteries.
2. The growing demand for sustainable energy storage stands out as AZIBs present cost-effective, safe, and environmentally friendly alternatives to lithium-ion batteries. Furthermore, the critical role played by Mn/V-based cathodes cannot be overlooked.
3. Advanced composite designs can enhance cathode performance and reduce resource use, while AI-guided material discovery can accelerate the development of eco-friendly cathodes. This review offers a framework for sustainable battery material design and promotes cleaner synthesis routes in energy storage, aligning with global sustainability goals.

1. Introduction

Compared with lithium-ion batteries, AZIBs, as a new energy storage technology, show the following obvious advantages:[1,2] (1) the zinc element has abundant resources, its theoretical mass specific capacity (820 mAh g^{-1}) and volume specific capacity (5855 mAh cm^{-3}) are high, and its redox potential is relatively low (−0.76 V *vs.* standard hydrogen electrode (SHE)). (2) Aqueous electrolytes exhibit high ionic conductivity, safety and environmental friendliness. (3) AZIBs have good anti-assembly conditions in an air atmosphere, are easy to prepare, and have low cost.

However, the lack of high-performance cathode materials is one of the challenges in the development of AZIBs.[3,4] At present, research on cathode materials mainly includes manganese-based oxides,[5,6] vanadium-based oxides,[7,8] Prussian blue analogues,[9,10] olivine-based phosphates,[11] Chevrel phase compounds,[12] and quinone derivatives.[13] Among them, V-based oxides and Mn-based compounds are the most studied materials due to their high zinc storage capacity, abundant valence states and high theoretical capacity. However, these materials face the drawbacks of poor rate and cycle performances, which are mainly due to their low intrinsic electronic conductivity, slow ion migration kinetics

[a]*School of New Energy Materials & Chemistry, Leshan Normal University, Leshan, Sichuan, 614000, P. R. China*
[b]*Institute for Materials Science and Devices, School of Materials Science & Engineering, Suzhou University of Science & Technology, Suzhou 215011, P. R. China. E-mail: ycbai@usts.edu.cn, zhangheng@usts.edu.cn*

and the dissolution of vanadium during cyclic charge–discharge.

In view of the above problems, researchers have coated or grown another phase on the surface of electrode materials to form composite materials to achieve the purpose of improving the electrochemical performance of materials.[14,15] At present, the most common way is to simply combine carbon-based materials, organic polymers, oxides and other conductive materials with electrode materials, which can play a role in promoting charge/electron transport dynamics, buffering stress changes and alleviating material dissolution.[14] Herein, we review the recent progress in using composite strategies to improve the electrochemical performance of vanadium-based/manganese-based cathode materials, including carbon nanotubes (CNTs), reduced graphene oxide (rGO), metal–organic framework (MOF)–derived carbon, MXenes and other compound carriers (Fig. 1). Green methods for the preparation of these composites are described, and the mechanism for performance enhancement is revealed. Furthermore, the future research and development direction of high-performance AZIBs cathode materials is prospected. It is expected that this review will provide more direct and powerful research directions for researchers.

2. Crystal structure characteristics of vanadium-based/manganese-based materials

2.1. Crystal structure characteristics of vanadium-based materials

2.1.1. VO_2. Vanadium-based compounds have been widely used in AZIBs in recent years due to the rich chemical valence states of vanadium, which can be continuously adjusted from 0 to +5 and realize multi-electron transfer in the process of redox reactions.[16] Vanadium-based compounds as cathode materials can be roughly divided into vanadium oxides, vanadates and vanadium chalcogenides in the well-known AZIBs (Fig. 2). Among the vanadium oxides, VO_2 has become the preferred cathode material for aqueous zinc-ion batteries because of its unique tunnel structure and high electrode potential. VO_2 has various crystal structures, including tetragonal vanadium dioxide (A-VO_2), monoclinic vanadium dioxide (B-VO_2, D-VO_2, and M-VO_2) and rutile vanadium dioxide (R-VO_2).[16] Among them, B-VO_2 has a layered structure composed of VO_6 edge-sharing octahedra, which is conducive to the rapid deintercalation of Zn^{2+}, and thus has become the most commonly used cathode material for batteries.

2.1.2. V_2O_5. In addition, the crystal structure of V_2O_5 is a layered structure, which is suitable for the intercalation/deintercalation of zinc ions between its layers. In addition, the multi-valence nature of vanadium and its relatively low relative atomic mass also contribute to its high theoretical specific capacity. However, the high charge density of zinc ions will have a strong electrostatic repulsion with the lattice of the host material during the de-intercalation process, which will lead to the destruction of the material structure, and then affect the cycle stability of the battery. In addition to VO_2 and V_2O_5, in recent studies, the vanadium oxides as cathode materials for AZIBs also include V_2O_3,[17] $H_2V_3O_8$ [18] and V_6O_{13},[19] which have distinct advantages as cathode materials for aqueous zinc-ion batteries.

2.1.3. Vanadate. Vanadate is a type of material formed by the intercalation of ions into vanadium oxides, which has attracted increasing attention because of its rich chemical reaction properties and good electrochemical properties. In recent years, as a new type of electrochemical material, vanadate nanomaterials (mainly include $M_xV_2O_5$, $M_xV_3O_8$, and $M_xV_2O_7$)[18,20] have better electrochemical performance and higher energy storage density, but most of them have poor stability during zinc ion intercalation and deintercalation.

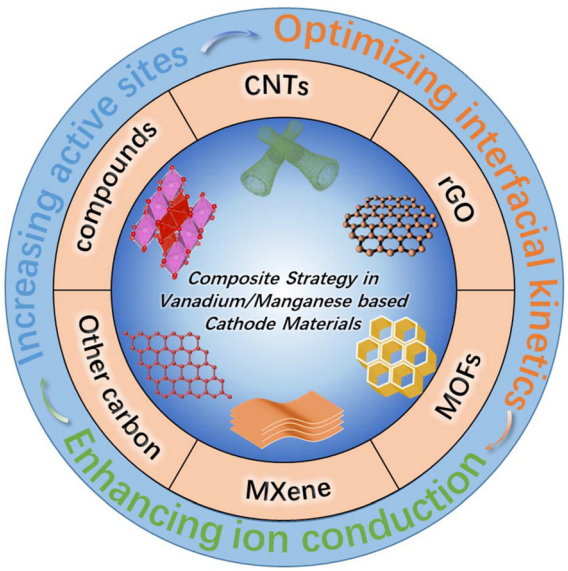

Fig. 1 Illustration of the composite strategy for vanadium-based/manganese-based materials.

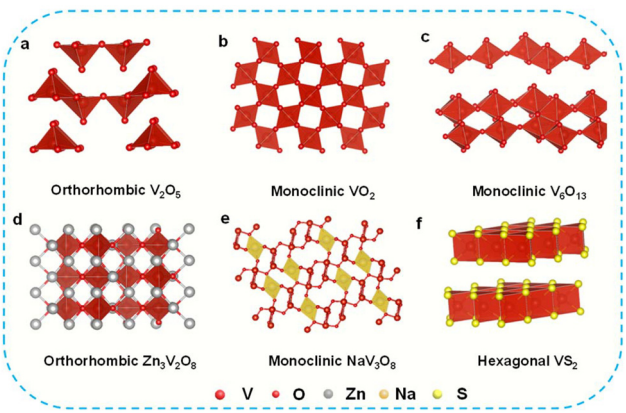

Fig. 2 Crystal structure of V_2O_5, VO_2, V_6O_{13}, $Zn_3V_2O_8$, NaV_3O_8, VS_2.

Therefore, some strategies are needed to improve their electrochemical performance.

2.1.4. Vanadium chalcogenide. Vanadium disulfide/vanadium diselenide (VS_2/VSe_2) and vanadium tetrasulfide (VS_4) are commonly used as cathode materials. The structure of VS_2/VSe_2 is similar to the layered structure of graphene, which has a large interlayer spacing, and this large interlayer spacing can be used for the free deintercalation of Zn^{2+} in the material during energy storage.[21] There is a vanadium layer between the two sulfur/selenium layers, forming a sandwich structure.

2.1.5. VN. Vanadium nitride has attracted significant attention due to its excellent electrical conductivity and high theoretical capacity, and has been widely used in catalysis, supercapacitors, preparation of vanadium steel and other fields. Generally, vanadium nitride is available in three forms, VN, V_2N, and V_3N. Among them, V_3N belongs to the hexagonal system. Alternatively, VN is an isomer of VC and VO with a face-centered cubic structure. The lattice spacing of VN is 0.146 nm, which is larger than the diameter of the zinc ion (0.074 nm). At the same time, VN has good conductivity and spatial structure, making it a good cathode material for aqueous zinc-ion batteries.[22] Generally, this open crystal structure not only provides a larger area for contact between the electrode material and the electrolyte, but also effectively shortens the electron/ion transport distance and provides more active sites, which are conducive to the rapid insertion and extraction of Zn^{2+}.

2.2. Crystal structure characteristics of manganese-based materials

Manganese-based compounds have attracted interest from a large number of researchers due to their unique advantages such as abundant reserves, environmental friendliness, low price, low toxicity and multi-valence (Mn^0, Mn^{2+}, Mn^{3+}, Mn^{4+} and Mn^{7+}). Mn has a variety of stable compounds such as MnO, Mn_3O_4, Mn_2O_3, MnO_2, MnO_3, and Mn_2O_7 [23] (Fig. 3).

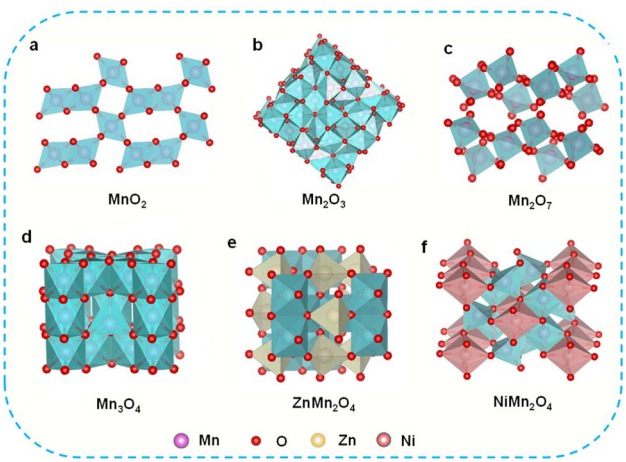

Fig. 3 Crystal structure of MnO_2, Mn_2O_3, Mn_2O_7, Mn_3O_4, $ZnMn_2O_4$, $NiMn_2O_4$.

2.2.1. MnO_2. The electrochemical performance of manganese dioxide depends on its crystal structure. α-MnO_2 belongs to the tetragonal system, which consists of eight MnO_2 molecules forming a unit cell, and six oxygen ions forming an octahedron around a manganese ion. In the *c*-axis direction, the [MnO_6] octahedra form double chains by sharing edges, and the adjacent octahedral double chains form a tunnel structure with a size of [2 × 2] by sharing vertices and pore size of about 4.66 Å.[24] β-MnO_2 also belongs to the tetragonal system, which exists in the form of pyrolusite in nature. It has high thermal stability and its crystal structure is not easily destroyed with an increase in temperature. Each unit cell contains two MnO_2 molecules. In the *c*-axis direction, the [MnO_6] octahedra are connected to form single chains, and then the octahedral single chains are stacked to form a [1 × 1] pore structure, and there is generally no bound water in the pore.[25] γ-MnO_2 belongs to the orthorhombic system, which is a close-packed hexagonal structure composed of a [1 × 1] single chain of pyrolusite and [2 × 1] double chain of ramsdellite, in which the ratio of the [1 × 1] to [2 × 1] tunnels is about 7 : 3. There are four MnO_2 molecules in each unit cell, and its pore structure is large, which is conducive to ion diffusion and high electrochemical activity, and because of its low cost, it is widely used in industrial production.[26] The structure of ε-MnO_2 is very similar to that of γ-MnO_2, but its stability is not the same. It is a metastable phase composed of [MnO_6] and [YO_6] octahedra (Y stands for defect). In this phase, Mn^{4+} accounts for 50% of the hexagonal close-packed octahedra, and the tunnel shape is irregular.[27] δ-MnO_2 belongs to the orthorhombic system and has a two-dimensional layered structure. In general, cations and water molecules are intercalated in its interlayer. Different intercalation mechanisms and ions in the interlayer lead to different types of δ-MnO_2.[28] λ-MnO_2 is a three-dimensional network spinel structure, where its oxygen coordination atoms form a square dense packing structure, its basic unit is an [MnO_6] octahedron, and its structure is a three-dimensional connected tunnel structure.[29]

2.2.2. Other oxides of manganese. In addition to MnO_2, other manganese-based oxides also show good a zinc storage performance as cathode materials. Spinel oxides with the molecular formula of AB_2O_4, including $ZnMn_2O_4$[30] and $NiMn_2O_4$[31] have been widely studied. As a type of zinc-manganese composite oxide, $ZnMn_2O_4$ has a stable crystal structure with zinc and manganese ions occupying different positions in its spinel structure, respectively. This structure endows $ZnMn_2O_4$ with good cycle stability and high specific capacity in zinc-ion batteries. In addition, the preparation of $ZnMn_2O_4$ is relatively simple and inexpensive, and thus it has broad application prospects in the field of aqueous zinc-ion batteries. $NiMn_2O_4$ is another spinel oxide with the formula AB_2O_4, in which nickel and manganese ions also occupy different positions in its spinel structure. As a cathode material, $NiMn_2O_4$ also shows a good electrochemical performance in AZIBs. Compared with $ZnMn_2O_4$, $NiMn_2O_4$ has a higher theoretical specific capacity and better rate capability.

3. Overview of composite strategy of vanadium-based/manganese-based materials for AZIBs

At present, a large number of studies in the literature (Table 1) have reported the strategy of improving the electrochemical performance of materials by compounding them with carbon/non-carbon materials to improve their shortcomings of easy dissolution and poor cycle stability. Their synthesis methods predominantly employ environmentally friendly approaches such as hydrothermal synthesis, mechanical ball milling, and electrochemical techniques to achieve efficient preparation and resource recycling. Their specific synthesis methods and performance enhancement mechanisms will be described in detail.

3.1. CNT/vanadium-based materials

CNTs are ideal reinforcements for the preparation of metal matrix composites due to their large specific surface area, abundant active sites, high conductivity and good mechanical elasticity. CNTs have unique advantages in the field of electrochemical energy storage,[32–34] as follows: (1) their large specific surface area can provide more active sites and enhance the reaction activity. (2) The good network structure of CNTs can provide abundant transmission channels for Faraday reactions. (3) The confinement effect of CNTs is conducive to avoiding the crushing and shedding of the active materials and ensuring cycle stability. (4) The interfacial interaction between CNTs and nanoparticles can effectively reduce the size of the particles and cause them to be uniformly dispersed. These unique structural advantages of CNTs are expected to enable composites to achieve electrochemical energy storage with higher energy density and power density at high rates. For example, to improve the cycle life of $KV_3O_8{\cdot}0.75H_2O$ (KVO) in AZIBs, Niu *et al.* prepared KVO/SWCNT composite films *via* a simple green hydrothermal method (Fig. 4a).[32] The network structure in the films ensured efficient electron transfer and intimate contact between KVO and SWCNTs during cycling. In addition, the KVO/SWCNT cathode exhibited a Zn^{2+}/H^+ insertion/extraction mechanism, resulting in fast ion transfer kinetics and an effective improvement in cycle life (Fig. 4b). Chen's group incorporated $Mn_{0.19}V_2O_5{\cdot}2.34H_2O$ (MnVOH) into a single-walled carbon nanotube (SWCNT) network (Fig. 4c).[33] Due to the close interaction between MnVOH and SWCNT in the nanocomposite, the continuous network structure and the expanded interlayer spacing facilitated fast electron transfer kinetics. Moreover, the CV curves (Fig. 4d) reveal that the voltage gap of MnVOH@SWCNTs (5 wt% SWCNTs) is much smaller than that of MnVOH, which can be attributed to the highly conductive SWCNTs, favoring faster ion diffusion and better electrochemical reaction kinetics. Too much or too little SWCNTs is not conducive to electrochemical energy storage. Xu *et al.* fabricated a self-supported hierarchical porous composite composed of double-layered $Na_xV_2O_5{\cdot}nH_2O$ (NVO) nanoribbons, CNTs and rGO with a three-dimensional cross-linked structure *via* a facile hydrothermal self-assembly method (Fig. 4e).[34] The unique hierarchical nanostructure of the hybrid one-dimensional (1D) (NVO nanoribbons) and 3D (rGO/CNT) scaffolds provides an efficient pathway for ion/electron transport and an elastic medium for large volume changes in the bilayer NVO nanoribbons during cycling (Fig. 4f). Rao *et al.* also prepared a $V_2O_5{\cdot}nH_2O$, GO and CNT composite membrane (HVO/GO-CNTs) *via* freeze-drying, which exhibited an excellent zinc storage performance.[35] Electrochemical performance tests showed that HVO and HVO/GO-CNTs have similar initial discharge capacities. However, the capacity of the HVO/GO-CNT film was much higher than that of the HVO film after 100 charge–discharge cycles (Fig. 4g). It was proven that GO and CNTs can effectively improve the cycle life of electrode materials. Ba *et al.* prepared a $V_3O_7{\cdot}H_2O$@CNT composite *via* the hydrothermal method, and used it as a cathode material in AZIBs to study the effect of carbon nanotubes on the microstructure and electrochemical performance of $V_3O_7{\cdot}H_2O$.[36] It can be seen from the SEM image that the CNTs are uniformly attached to the $V_3O_7{\cdot}H_2O$ nanowires (Fig. 4h). The rate test also proved that the addition of CNTs reduced the electrochemical polarization in the composite material (Fig. 4i), and the addition of CNTs could accelerate electron transfer. The above-mentioned studies fully confirm that carbon nanotubes can not only significantly improve the conductivity, enhance the structural stability and accelerate charge transport in the electrode, but also the green synthesis process for carbon nanotube-based composites is in line with the requirements of sustainable development, which improves the electrochemical performance and achieves environmental friendliness.

3.2. CNT/manganese-based materials

Wang *et al.* developed a cable-type flexible rechargeable zinc microbattery based on a micron-sized MnO_2@carbon nanotube fibrous composite cathode and zinc wire anode (Fig. 5a).[37] The Zn-MnO_2 cable cells could be folded into arbitrary shapes without sacrificing their electrochemical performance due to the flexibility of CNT, which exhibited excellent flexibility. The assembled Zn-MnO_2 cable microbattery exhibited a high specific capacity, good rate capability and cycle stability (Fig. 5b). In addition to the composite materials of MnO_2 and CNT, Mn_3O_4 was composited with CNT to improve its electrochemical performance. For example, Guo *et al.* achieved an excellent electrochemical performance by growing manganese-deficient Mn_3O_4 nanoparticles *in situ* on highly conductive CNTs (denoted as DMOCs) as cathode materials for aqueous rechargeable zinc-ion batteries (RAZIB).[38] The DMOC cathode combines the advantages of Mn-rich defects, small particle size and CNT structure. These features not only enhance the electronic conductivity and structural stability, but also generate more active sites and contribute to fast reaction kinetics. As displayed in Fig. 5c, the DMOC material achieved the highest capacity of 420.6 mAh g^{-1} at 0.1 A g^{-1}. Also, it exhibited an excellent cycle life of 2800 cycles at 2.0 A g^{-1} with a high-capacity retention of 84.1% (Fig. 5d). In

Table 1 Review of recently reported vanadium-based and manganese-based cathode materials using composite strategies for AZIBs

Materials	Electrolytes	Remaining capacity (mAh g^{-1}) (current density, cycles)	Synthetic method	Ref.
KVO/SWCNT	4 M $Zn(CF_3SO_3)_2$	200 (5 A g^{-1}, 10000 cycles)	Hydrothermal	32
MnVOH@SWCNT	3 M $Zn(CF_3SO_3)_2$	324 (5 A g^{-1}, 300 cycles)	Hydrothermal	33
$Na_xV_2O_5{\cdot}nH_2O$/rGO/CNT	3 M $Zn(CF_3SO_3)_2$	301.9 (10 A g^{-1}, 1800 cycles)	Hydrothermal	34
HVO/GO-CNTs	3 M $Zn(CF_3SO_3)_2$	261 (1 A g^{-1}, 100 cycles)	Sol–gel	35
$V_3O_7{\cdot}H_2O$@CNTs	3 M $Zn(CF_3SO_3)_2$	297.8 (10 A g^{-1}, 1500 cycles)	Hydrothermal	36
MnO_2@CNT	$ZnCl_2$ gel polymer	62 (2 A g^{-1}, 2 cycles)	Chemical-vapor-Deposition	37
Mn_3O_4/CNTs	2 M $ZnSO_4$ + 0.2 M $MnSO_4$	75.4 (2 A g^{-1}, 2800 cycles)	Solvothermal	38
Mn_3O_4@CNT-CNT	2 M $ZnSO_4$ + 0.1 M $MnSO_4$	234 (1 A g^{-1}, 400 cycles)	Solvothermal	39
$ZnMn_2O_4$/CNTs	2 M $ZnSO_4$ + 0.2 M $MnSO_4$	151 (0.5 A g^{-1}, 100 cycles)	Reflux	40
A-V_2O_5/G	3 M $ZnSO_4$	276 (10 A g^{-1}, 800 cycles)	Solvothermal	41
VrGO@V_2O_5	2 M $ZnSO_4$	329.8 (0.2 A g^{-1}, 1 cycles)	Electrochemical deposition	42
$FeVO_4{\cdot}nH_2O$@rGO LaVO/rGO	2 M $Zn(TFSI)_2$	≈100 (1 A g^{-1}, 1000 cycles)	Hydrothermal	43
$Na_{1.1}V_3O_{7.9}$@rGO	3 M $ZnSO_4$	144 (8 A g^{-1}, 6000 cycles)	Hydrothermal	44
O_d-HVO/rG	1 M $Zn(CF_3SO_3)_2$	171 (0.3 A g^{-1}, 100 cycles)	Solvothermal	45
VN-rGO	3 M $ZnSO_4$	197.5 (10 A g^{-1}, 2000 cycles)	Hydrothermal	46
rGO-VSe_2	2 M $Zn(CF_3SO_3)_2$	445 (1 A g^{-1}, 400 cycles)	Spray pyrolysis Hydrothermal	47
VS_4@rGO	2 M $ZnSO_4$	213.8 (0.5 A g^{-1}, 150 cycles)	Hydrothermal	48
G-MnO_2	1 M $Zn(CF_3SO_3)_2$	180 (1 A g^{-1}, 165 cycles)	Hydrothermal	49
VG-MnO_2-PEDOT:PSS	2 M $ZnSO_4$ + 0.1 M $MnSO_4$	294.5 (0.048 A g^{-1}, 100 cycles)	Hydrothermal	50
B-MnO_2@GO	1 M $ZnSO_4$ + 0.1 M $MnSO_4$	367.4 (0.5 A g^{-1}, 1 cycles)	Hydrothermal	51
A-MnO/G	3 M $ZnSO_4$ + 0.2 M $MnSO_4$	≈129.6 (1.232 A g^{-1}, 2000 cycles)	Static oxidation method	52
MnSe@rGO	3 M $ZnSO_4$ + 0.1 M $MnSO_4$	77 (3 A g^{-1}, 2000 cycles)	Hydrothermal	53
a-V_2O_5@C	2 M $ZnSO_4$ + 0.1 M $MnSO_4$	290 (0.1 C, 100 cycles)	Solvothermal	54
a-V_2O_5@C	3 M $Zn(CF_3SO_3)_2$	249.2 (40 A g^{-1}, 20 000 cycles)	*in situ* electrochemically oxidation	55
C@VO_2@V_2O_5	3 M $ZnSO_4$	448 (0.15 A g^{-1}, 5 cycles)	Solvothermal	56
V_2O_5@CNT	2 M $ZnSO_4$	167 (5 A g^{-1}, 2000 cycles)	Solvothermal	57
N/C@V_2O_3	3 M $Zn(CF_3SO_3)_2$	238 (1 A g^{-1}, 2000 cycles)	Hydrothermal	58
	2 M $ZnSO_4$	293.8 (1 A g^{-1}, 500 cycles)		59
$Cu_{0.26}V_2O_5$@C	3M $Zn(CF_3SO_3)_2$	173.5 (2 A g^{-1}, 500 cycles)	Hydrothermal	60
MnO_x@N–C	$ZnSO_4$ + $MnSO_4$	305 (0.5 A g^{-1}, 600 cycles)	Solvothermal	61
Mn-H_3BTC-MOF	2 M $Zn(CF_3SO_3)_2$	138 (0.1 A g^{-1}, 100 cycles)	Solvothermal	62
Mn-MOF/CNT	2 M $ZnSO_4$ + 0.1 M $MnSO_4$	170 (0.1 A g^{-1}, 60 cycles)	Solvothermal	63
N-doped C/V_2O_3	3 M $ZnSO_4$	402.4 (0.1 A g^{-1}, 152 cycles)	Electrostatic spinning	64
V_2O_3@C	3 M $Zn(CF_3SO_3)_2$	202 (5 A g^{-1}, 2000 cycles)	Solvothermal	65
V_2O_3/CCN	3 M $ZnSO_4$	215.93 (3 A g^{-1}, 58 cycles)	Evaporation-induced self-assembly	66
VO_2@NC	3 M $Zn(CF_3SO_3)_2$	268.5 (10 A g^{-1}, 2500 cycles)	Calcining	67
ZnV_2O_4/C–N	2 M $ZnSO_4$	82 (2 A g^{-1}, 1000 cycles)	Stirring	68
$VOPO_4$/C	2 M $Zn(CF_3SO_3)_2$	120 (0.5 A g^{-1}, 100 cycles)	Reflux	69
$Na_3V_2(PO_4)_3$@C	2 M $Zn(CF_3SO_3)_2$	≈98.9 (0.1 A g^{-1}, 10 cycles)	Sol–gel	70
MnO@C	3 M $ZnSO_4$	250 (0.1 A g^{-1}, 30 cycles)	Hydrothermal	71
MnO@C	2 M $ZnSO_4$ + 0.2 M $MnSO_4$	128 (2 A g^{-1}, 2000 cycles)	Solvothermal	72
ε-MnO_2@C	2 M $ZnSO_4$ + 1 M $MnSO_4$	172 (1 A g^{-1}, 1700 cycles)	Stirring	73
GC-δ-MnO_2	2 M $ZnSO_4$ + 0.1 M $MnSO_4$	277.2 (0.3 A g^{-1}, 100 cycles)	Stirring	74
MnO_2@NC	2 M $ZnSO_4$ + 0.2 M $MnSO_4$	≈84.6 (2 A g^{-1}, 2500 cycles)	Hydrothermal	75
δ-MnO_2-HCF	2 M $ZnSO_4$ + 0.3 M $MnSO_4$	117.2 (2 A g^{-1}, 3500 cycles)	Hydrothermal	76
V_2O_x@V_2CT_x	1 M $ZnSO_4{\cdot}7H_2O$	≈81.6 (1 A g^{-1}, 200 cycles)	High-temperature etching method	77
V_2O_5-MXen	3 M $Zn(CF_3SO_3)_2$	≈99.5% (10 A g^{-1}, 500 cycles)	Self-assembly	78
ZnVO	3 M $Zn(CF_3SO_3)_2$	184 (5 A g^{-1}, 15 000 cycles)	Hydrothermal	79
$CeVO_4$/V_2CT_xMXene	3 M $ZnSO_4$	240.3 (1 A g^{-1}, 200 cycles)	Hydrothermal	80
VS_2/MXene	2 M $ZnCl_2$	93.4% (5 A g^{-1}, 2400 cycles)	Hydrothermal	81
MXene@MnO_2	2 M $ZnSO_4$ + 0.1 M $MnSO_4$	≈255 (0.5A g^{-1}, 2000 cycles)	Gas-phase spray drying approach	82
K-V_2C@MnO_2	2 M $ZnSO_4$ + 0.25 M $MnSO_4$	119.2 (10 A g^{-1}, 10 000 cycles)	Hydrothermal	83
MnO_2/MXene	2 M $ZnSO_4$ + 0.1 M $MnSO_4$	290.8 (0.2 A g^{-1}, 200 cycles)	Stirring	84
ZMO@$Ti_3C_2T_x$	1 M $ZnSO_4$	≈119.5 (1 A g^{-1}, 2000 cycles)	Solvothermal	85
NMO/MXene	2 M $ZnSO_4$ + 0.1 M $MnSO_4$	289 (1.54 A g^{-1}, 2500 cycles)	Molten salt	86
$V_2O_5{\cdot}3H_2O$@VS_2	3 M ZnSO4	240 (5 A g^{-1}, 4000 cycles)	Hydrothermal	87
V_6O_{13}/$CeVO_4$	3 M $Zn(CF_3SO_3)_2$	280 (1 A g^{-1}, 300 cycles)	Hydrothermal	88
$Mn(VO_3)_2$/$NaVO_3$	3 M ZnSO4	231.8 (5 A g^{-1}, 1000 cycles)	Hydrothermal	89
VN/V_3S_4	3 M $Zn(CF_3SO_3)_2$	115.4 (10 A g^{-1}, 4000 cycles)	Solvothermal	90
V_2O_3-VN	3 M $ZnSO_4{\cdot}7H_2O$	114.5 (3 A g^{-1}, 4800 cycles)	Stirring	91

addition, the highly reversible zinc ion intercalation and deintercalation mechanism and high structural stability of DMOC were also confirmed by *ex situ* XRD (Fig. 5e–g). Furthermore, to improve the rapid capacity fading and poor rate performance of Mn_3O_4, Tong *et al.* prepared a composite material of Mn_3O_4 with a size of 8–10 nm coated on ZIF-8-CNT, and obtained an Mn_3O_4@CNT-CNT composite with a double carbon nanotube structure after calcination.[39] As the cathode material of AZIBs,

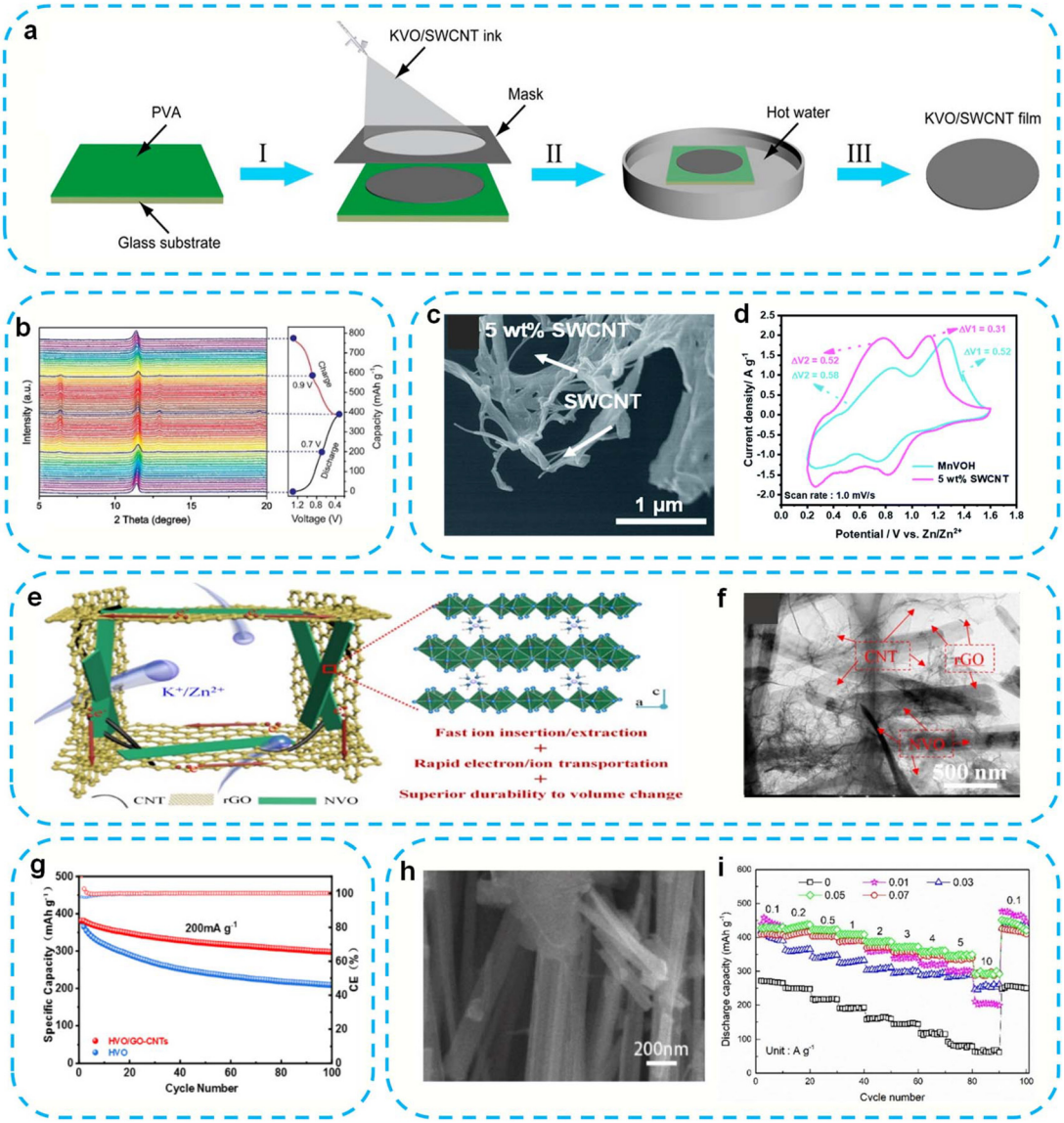

Fig. 4 Schematic of the KVO/SWCNT (a). *In situ* XRD patterns of the KVO/SWCNT electrode during charge/discharge process (b). (a and b) Reproduced with permission.[32] Copyright 2020, the American Chemical Society. FESEM images of MnVOH@SWCNTs (c). CV curve of MnVOH@SWCNTs (d). (c and d) Reproduced with permission.[33] Copyright 2022, the Royal Society of Chemistry. Schematic of the NVO/rGO/CNT (e). TEM images of the NVO/rGO/CNT composite (f). (e and f) Reproduced with permission.[34] Copyright 2020, the American Chemical Society. Cycling performance of HVO/GO-CNTs and HVO (g). (g) Reproduced with permission.[35] Copyright 2024, Wiley-VCH. SEM images of VOH@C-0.05 (h). Rate performance of VOH@C-0.05 (i). (h and i) Reproduced with permission.[36] Copyright 2024, Elsevier.

this composite exhibited excellent electrochemical properties, which are better than that of most manganese matrix composites, showing a discharge capacity of 234 mAh g^{-1} at 1 A g^{-1} after 400 cycles (Fig. 5h). The diffusion coefficient of zinc ions in Mn_3O_4@CNT-CNT is also higher than that of Mn_3O_4-based composites by compounding with carbon nanotubes (Fig. 5i). Yang *et al.* synthesized sulfur-doped $ZnMn_2O_4$/CNT composites (S-$ZnMn_2O_4$/CNTs) by combining the sulfur-doping strategy with the composite strategy (Fig. 5j).[40] The AZIBs assembled using the as-prepared S-$ZnMn_2O_4$/CNTs exhibited excellent storage capacity and extended cycle life (Fig. 5k).

3.3. Graphene/vanadium-based materials

Graphene is a two-dimensional carbon nanomaterial with a hexagonal honeycomb lattice composed of carbon atoms with sp^2 hybrid orbitals.[41] Compared with other carbon materials, graphene has many excellent properties, such as high electron mobility, thermal conductivity, good flexibility and superior mechanical strength. Moreover, the theoretical specific surface area of graphene is much higher than that of one-dimensional carbon nanotubes and graphite materials, and thus it is considered an ideal electrode material for the next generation of

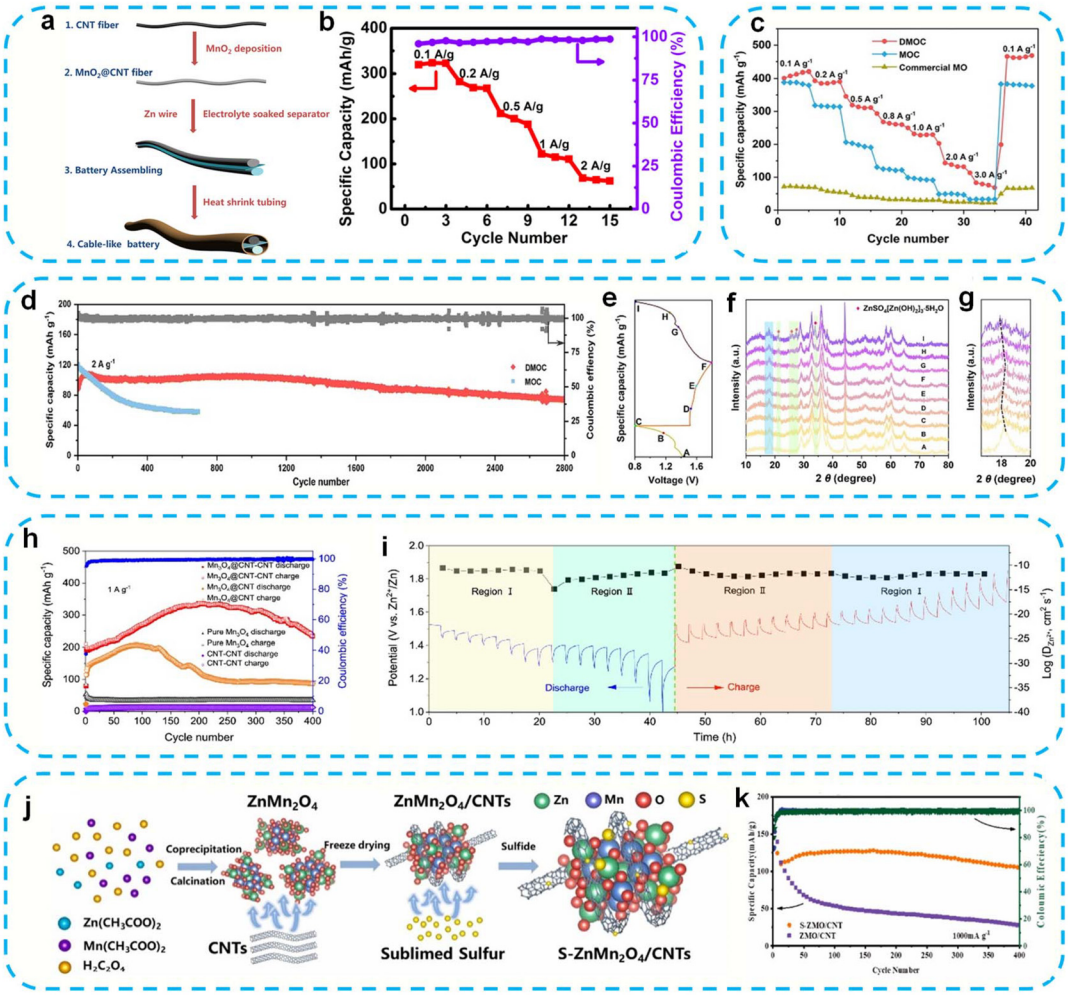

Fig. 5 Schematic of the preparation process of a Zn-MnO_2 cable battery based on an MnO_2@CNT fiber cathode and Zn wire anode (a). Specific capacity plots and coulombic efficiency of MnO_2-30@CNT fiber electrodes (b). (a and b) Reproduced with permission.[37] Copyright 2018, the American Chemical Society. Rate capability of DMOC (c). Cycling stability of DMOC (d). XRD patterns of the DMOC cathode in a typical GCD procedure (e–g). (c–g) Reproduced with permission.[38] Copyright 2022, Elsevier. Cycling performances of the Mn_3O_4@CNT-CNT (h). GITT profiles in the discharging and charging process (i). (h and i) Reproduced with permission.[39] Copyright 2022, Elsevier. Schematic diagram of the synthetic procedure of S-$ZnMn_2O_4$/CNTs (j). Cycling performance of S-$ZnMn_2O_4$/CNTs (k). (j and k) Reproduced with permission.[40] Copyright 2023, Elsevier.

electrochemical energy storage devices.[41] Some vanadium-based materials have been composited with graphene to improve their electrochemical performance. For example, Wang *et al.* synthesized a novel two-dimensional heterostructure by uniformly growing ultrathin amorphous vanadium pentoxide on graphene (A-V_2O_5/G).[41] It can be seen in Fig. 6a that the 2D V_2O_5/G heterostructure exhibits an ultrathin planar morphology with a nanosheet structure, and its lateral size can reach 10 μm. The prepared 2D heterogeneous material showed a high rate performance when used as a cathode material in AZIBs due to its very short ion diffusion path, abundant active sites, high conductivity and excellent structural stability. Subsequently, Zhong *et al.* proposed a V_2O_5 heterostructure coated with vertically aligned reduced graphene oxide (VrGO).[42] The results showed that the VrGO nanosheets can effectively inhibit the dissolution of V_2O_5 and provide channels for the effective transport of zinc ions and electrons, thus improving the electrochemical reaction kinetics of the electrode (Fig. 6b). As a result, VrGO@V_2O_5 exhibited an excellent rate performance (Fig. 6c). Lan *et al.* compounded $FeVO_4{\cdot}nH_2O$ and reduced graphene to obtain a high specific capacity and stable cycle life.[43] The structural stability of $FeVO_4{\cdot}nH_2O$@rGO and its reversible zinc ion extraction mechanism were also confirmed by *in situ* XRD (Fig. 6d). To improve the rate capability and cycle life of vanadium-based cathode materials, Wu *et al.* successfully synthesized an $La_{0.14}V_2O_5$/reduced graphene oxide composite (denoted as LaVO/rGO) *via* a simple hydrothermal method.[44] Due to the combination of the columnar La^{3+} ions and the highly conductive rGO, the layered LaVO/rGO exhibited a large interlayer spacing (14.77 Å) (Fig. 6e), which guaranteed the fast kinetics of Zn^{2+}/H^+ intercalation/deintercalation. Therefore, the LaVO/rGO composite

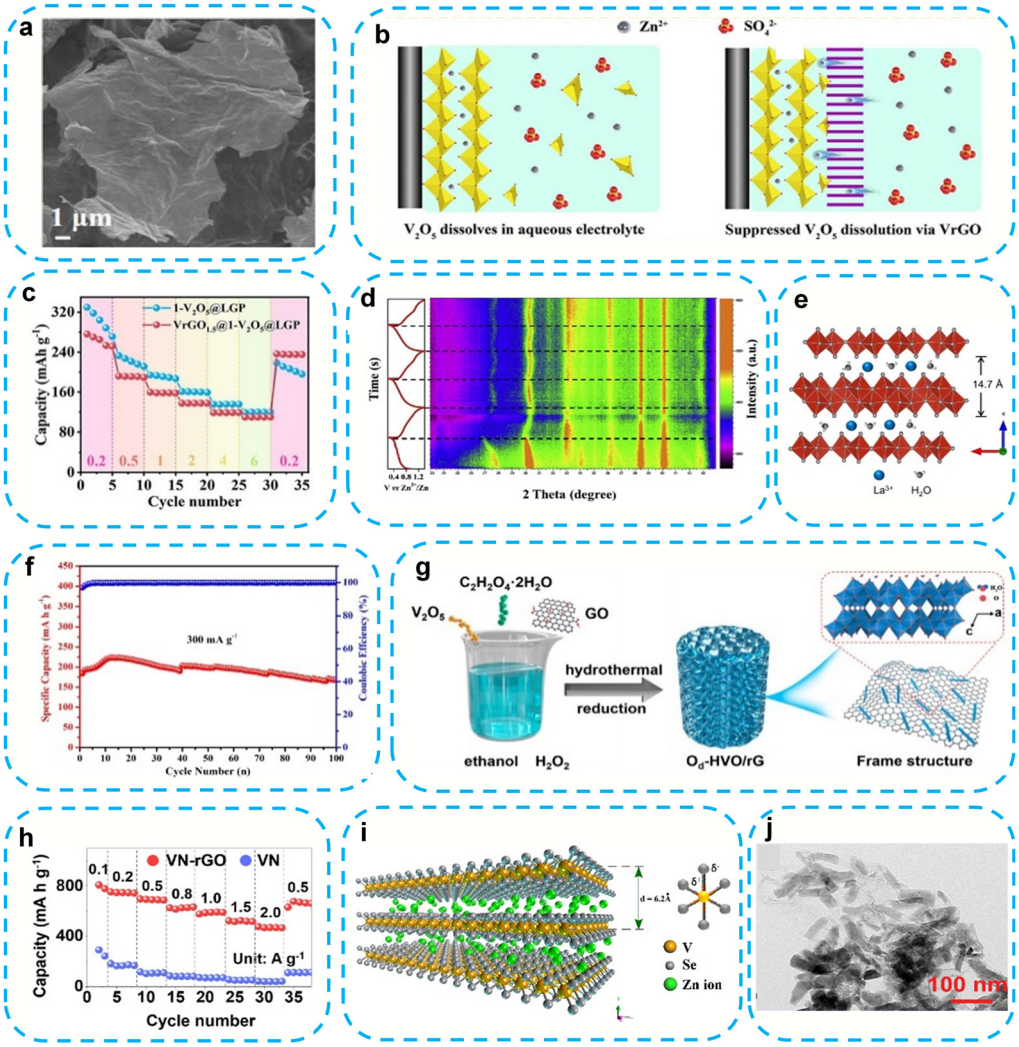

Fig. 6 SEM images of A-V_2O_5/G heterostructures (a). (a) Reproduced with permission.[41] Copyright 2020, Wiley-VCH. Illustration of V_2O_5 dissolved in a $ZnSO_4$ solution of $VrGO_{1.5}$@1-V_2O_5@LGP (b). Rate capability of $VrGO_{1.5}$@1-V_2O_5@LGP (c). (b and c) Reproduced with permission.[42] Copyright 2023, the American Chemical Society. 2D *in situ* XRD patterns of FVO@rGO (d). (d) Reproduced with permission.[43] Copyright 2020, Elsevier. Illustration of the LaVO structure (e). (e) Reproduced with permission.[44] Copyright 2021, The Electrochemical Society. Cycle performance of $Na_{1.1}V_3O_{7.9}$@rGO (f). (f) Reproduced with permission.[45] Copyright 2018, Elsevier. Hydrothermal reaction synthesis process for O_d-HVO/rGO (g). (g) Reproduced with permission.[46] Copyright 2021, the American Chemical Society. Rate performance of VN-rGO microspheres (h). (h) Reproduced with permission.[47] Copyright 2022, Elsevier. Schematic of Zn storage in an rGO-VSe_2 nanohybrid (i). (i) Reproduced with permission.[48] Copyright 2021, Elsevier. TEM image of VS_4@rGO (j). (j) Reproduced with permission.[49] Copyright 2018, the Royal Society of Chemistry.

exhibited a stable discharge capacity in 500 cycles with a capacity retention of 86%, which is much higher than that of LaVO (71%). In addition, the $Na_{1.1}V_3O_{7.9}$@rGO composite prepared by Cai *et al.* also exhibited an excellent zinc storage performance (Fig. 6f).[45] To further improve the electrochemical zinc storage performance of V-based materials, Huang *et al.* combined defect engineering and composite strategies to synthesize oxygen vacancy-rich O_d-HVO/rG composites *via* hydrothermal method (Fig. 6g).[46] The O_d-HVO/rG cathode exhibited a high capacity, and its capacity gradually increased during cycling due to the high conductivity of rGO nanosheets and the robust 3D sponge structure. In addition to vanadium oxide, graphene has also been used to improve the storage properties of transition metal chalcogenides. For example, Kang's research group synthesized porous VN-reduced graphene oxide composite (VN-rGO) microspheres with a unique structure through a simple spray pyrolysis process, and studied the electrochemical reaction mechanism of VN-rGO microspheres through *ex situ* characterization.[47] Owing to the high conductivity of 3D rGO and the VN encapsulated structure, the contact between the VN nanocrystals and the conductive matrix is maximized. In addition, the porosity of nanomaterials increases the contact between the electrode materials. Therefore, the composite material showed an excellent rate capability (Fig. 6h). In addition, Yan's group synthesized marigold-like reduced rGO and VSe_2 nanohybrids *via*

a one-step hydrothermal method.[48] This highly conductive rGO-coated VSe_2 can inhibit the electrostatic stacking of nanosheets, and simultaneously serve as a template to form marigold-like nanohybrid structures. In addition, the strongly conductive graphene provides a three-dimensional channel for electron transfer, which reduces the diffusion path for electrolyte ions and improves the reaction kinetics (Fig. 6i). Qin *et al.* also demonstrated that vanadium sulfide anchored on reduced graphene oxide (VS_4@rGO) prepared *via* a simple green hydrothermal method exhibited an excellent electrochemical performance.[49] It can be observed from the TEM image that the rice grain-like VS_4 (with a length of 70 nm and width of 30 nm) is anchored on the rGO matrix (Fig. 6j). Benefiting from the unique crystal structure of VS_4 and the superior conductivity of rGO, VS_4@rGO achieved a high capacity retention of 83.7%, showing an excellent rate performance. The above-mentioned studies confirm that graphene not only has high conductivity, but also can be used as a template to effectively reduce the size of nano-ions. By compounding with graphene, various electrode materials with unique structures can be prepared, and the electrochemical performance of the electrode materials can be effectively improved. At the same time, green synthesis methods such as hydrothermal treatment and spray pyrolysis are usually used in the preparation of graphene composites, which can reduce the environmental load and resource consumption in their preparation process.

3.4. Graphene/manganese-based materials

To improve the electrochemical performance of manganese-based materials, graphene is usually used to modify them. For example, Wang *et al.* synthesized a binder-free three-dimensional porous graphene aerogel-supported α-MnO_2 cathode (G-MnO_2) through a simple and scalable hydrogel method (Fig. 7a).[50] The G-MnO_2 hybrid aerogel effectively reduced the resistance of transporting Zn^{2+} ions and electrons due to its large pore structure and high surface area (Fig. 7b), while buffering the volume change of the α-MnO_2 nanotubes during repeated discharge/charge cycles. Subsequently, Chen *et al.* also improved the poor conductivity and charging kinetics of manganese dioxide by compounding it with graphene.[51] MnO_2 nanomaterials were embedded in a highly conductive network of vertical graphene (VG) nanosheets, where the 3D nanolabyrinth microstructure of the graphene nanosheets provided a conductive channel for fast electron and charge transfer. TEM also confirmed that the MnO_2 nanoparticles synthesized by this method were well dispersed without agglomeration (Fig. 7c). In addition, a flexible device was assembled and its electrochemical performance also tested. As shown in Fig. 7d, a high-performance flexible quasi-solid-state Zn-MnO_2 battery was prepared by sandwiching a polyvinyl alcohol (PVA) gel electrolyte between a VMP cathode and a Zn anode. Studies have demonstrated that quasi-solid-state batteries have significantly higher mechanical durability compared to aqueous systems. Secondly, the risk of electrolyte leakage is avoided, and dendrite formation and dissolution of the active material are limited. In addition, Ding *et al.* combined defect engineering and interface optimization to fabricate an oxygen-defect-rich β-MnO_2@graphene oxide cathode to improve the rate capability and cycling stability of the MnO_2 cathode.[52] The zinc ion and proton cointercalation mechanism of β-MnO_2@GO was also revealed by *in situ* XRD (Fig. 7e and f). In addition, Guo *et al.* fabricated an accordion-like heterostructure (A-MnO/G) with alternating layers of graphene and MnO nanosheets (Fig. 7g).[53] It was found that the covalent bonding of the graphene–MnO interface promoted the formation of vacancies/defects, resulting in a disordered phase of MnO, increasing the number of active sites in the material and obtaining a good electrochemical performance (Fig. 7h). As shown in Fig. 7i, it was found that the red area around Zn is not connected with other atoms, indicating that the adsorption is due to charge transfer rather than chemical bonding according to the theoretical simulation. To further improve the electrochemical performance of manganese-based materials, Tian's group proposed an AZIB cathode based on reduced graphene oxide (rGO)-coated MnSe nanoparticles (MnSe@rGO) (Fig. 7j).[54] The structural evolution of the material during the initial charge–discharge cycle was revealed by *in situ* Raman spectroscopy. As shown in Fig. 7k, the *in situ* Raman spectrum shows that MnSe was completely transformed into an MnO_2-like structure during the initial charge activation process, and the deintercalation of protons rather than zinc ions occurred during the subsequent charge–discharge process, which was also the reason for the excellent electrochemical performance.

3.5. MOF derivative/vanadium-based materials

Metal–organic frameworks (MOFs) are formed by bridging bonds (network synthesis) to establish strong links between inorganic and organic units. In the past decade, MOFs have been widely studied and reported due to their adjustable composition, various geometric shapes, and flexibility in terms of size and function. Organic ligands are usually symmetrical or polyhedral organic carboxylic acids. They produce a stable crystal MOF structure with a large specific surface area and porosity when they are connected with metal-containing units. Although significant achievements have been made in the direct application of MOF materials, in recent years, the research and application of MOF derivatives have attracted wide attention, especially in the field of energy storage. MOFs are characterized by structural diversity, porosity and compositional tunability, and thus as sacrificial templates, a variety of porous nanomaterials can be obtained *via* different thermal or chemical treatments. Heat treatment of MOFs in an inert atmosphere can retain their framework structure, while their organic components are carbonized *in situ*, and the metal ions on their surface are removed by chemical etching to produce porous carbon with a high specific surface area. Compared with porous carbon materials prepared using other precursors, MOF-derived carbon has a controllable framework structure, pore volume and specific surface area, making it very suitable for application in the electrochemical energy storage field such as supercapacitors and secondary batteries. For example, for

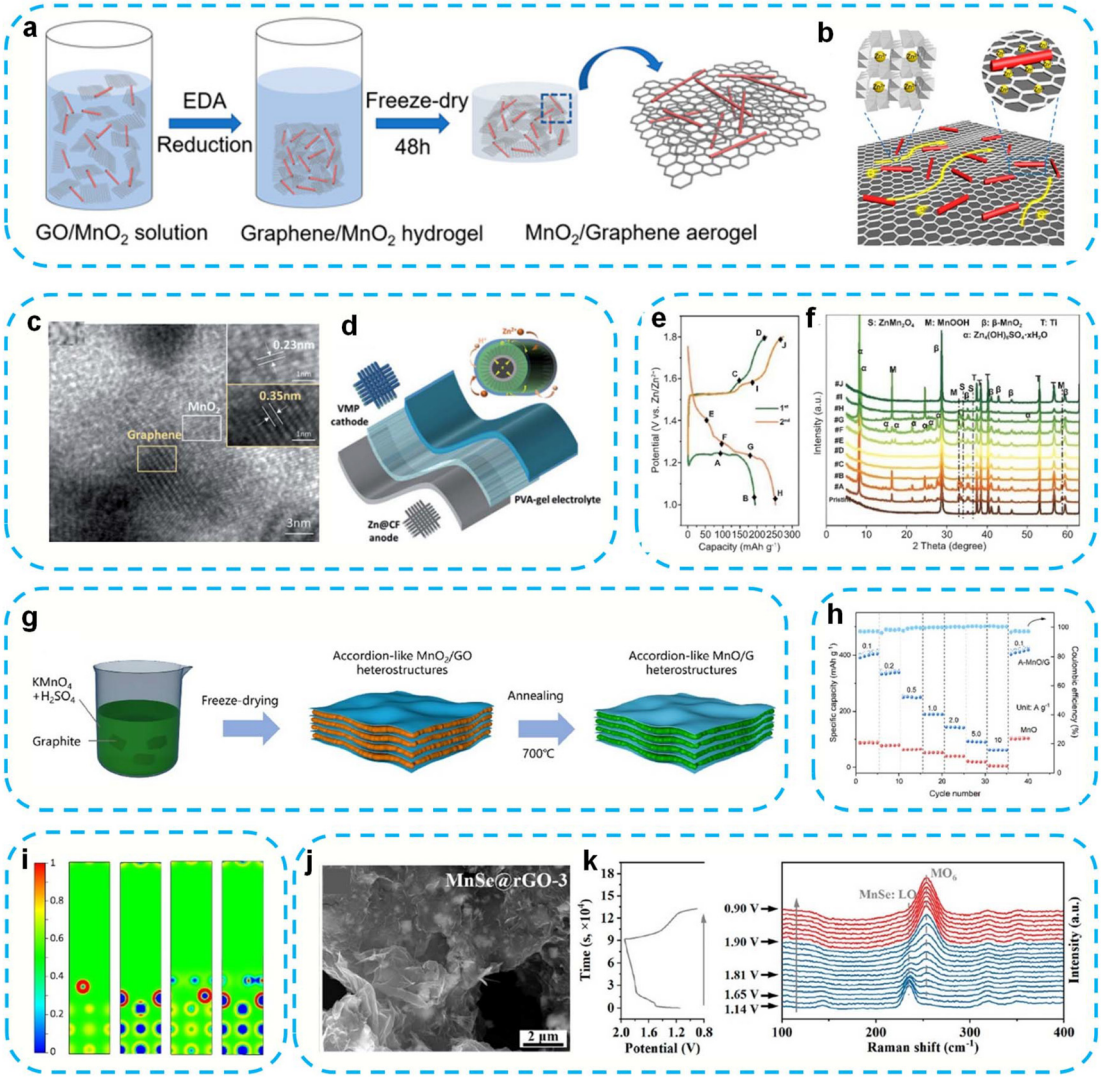

Fig. 7 Schematic of the process for the formation of G-MnO_2 (a). Graphical illustration of the structural merits and the integrated Zn^{2+} ion storage mechanisms in the G-MnO_2 electrode (b). (a and b) Reproduced with permission.[50] Copyright 2020, the American Chemical Society. HRTEM images of VG-MnO_2 (c). Schematic of a flexible quasi-solid-state Zn-VMP battery (d). (c and d) Reproduced with permission.[51] Copyright 2021, the Royal Society of Chemistry. *Ex situ* XRD patterns of β-MnO_2@GO (e and f). (e and f) Reproduced with permission.[52] Copyright 2021, Springer. Synthesis and structural analysis of A-MnO/G (g). Rate performance of β-MnO_2@GO (h). Electron cloud distributions of MnO, V-MnO, A-MnO/G and V-A-MnO/G (i). (g-i) Reproduced with permission.[53] Copyright 2022, Elsevier. SEM images of MnSe@rGO-3 (j). Potential profile and *in situ* Raman spectra of the MnSe@rGO-3 electrode (k). (j and k) Reproduced with permission.[54] Copyright 2023, the American Chemical Society.

the first time, the Niu research group prepared a composite material (a-V_2O_5@C) of amorphous V_2O_5 and MOF precursor carbon materials *via* electrochemical *in situ* induction, in which V_2O_5 was uniformly distributed in the carbon skeleton in the amorphous state (Fig. 8a).[55] The porous carbon framework provided a continuous electron transport pathway and an ion diffusion channel. Therefore, the a-V_2O_5@C composite exhibited an excellent electrochemical performance (Fig. 8b). This work provides a valuable reference for the design of AZIB cathodes with an excellent rate performance. Subsequently, Li *et al.* also used an *in situ* electrochemically induced method to prepare hollow nanotubular amorphous vanadium oxide and carbon (a-V_2O_5@C) hybrids (Fig. 8c and d),[56] and comprehensively studied their electrochemical performance as cathode materials for AZIBs. The a-V_2O_5@C hybrid material has abundant ion storage sites, isotropic ion diffusion paths, and excellent conductivity due to the unique amorphous structure of V_2O_5 and its close contact with carbon. In addition, Tong *et al.* successfully synthesized a mesoporous C@VO_2@V_2O_5 nanocomposite using a vanadium-based organic framework as a precursor through carbonization and subsequent oxidation processes.[57] It can be seen from the SEM images that the C@VO_2@V_2O_5 structure is a uniform nanorod structure with a smooth surface (Fig. 8e). Due to the abundant Zn^{2+} active sites and fast Zn^{2+} intercalation kinetics brought by the heterojunction structure and mesoporous structure of the two-phase

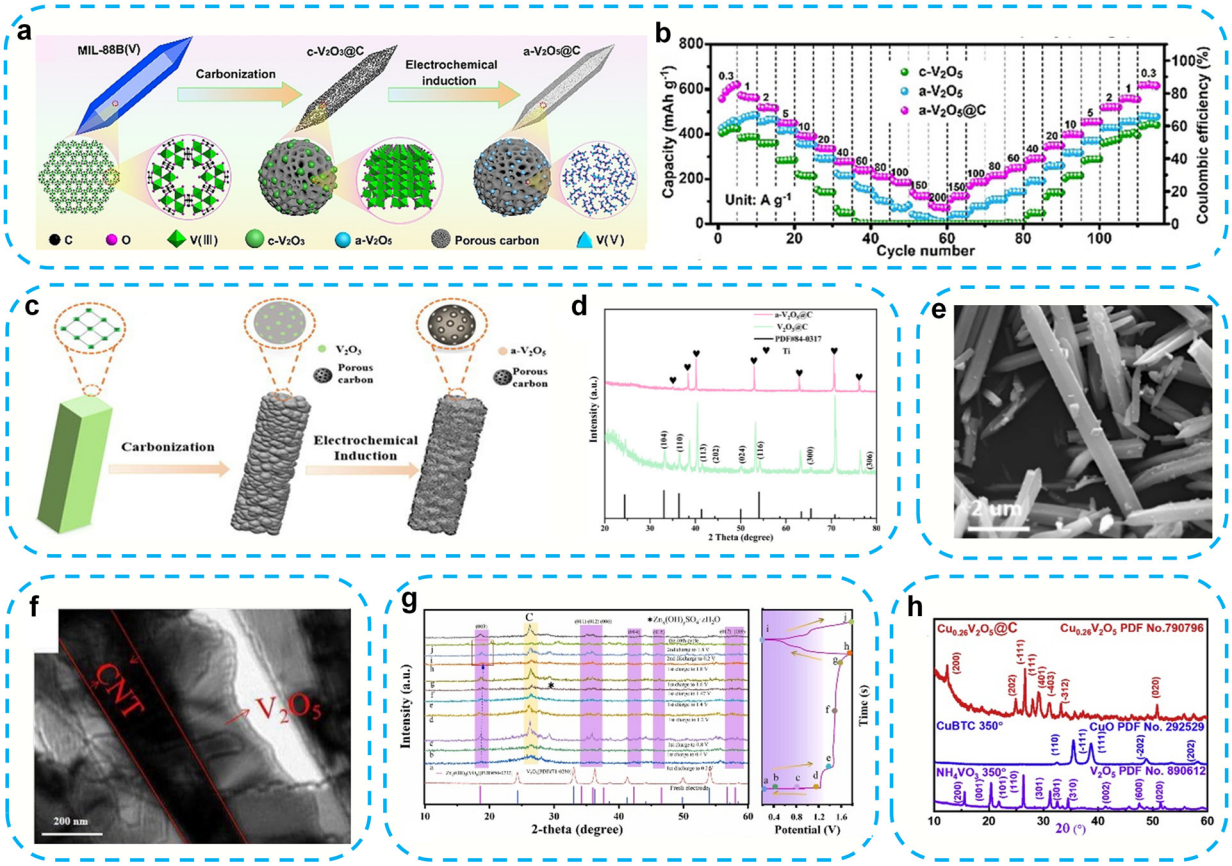

Fig. 8 Schematic of the fabrication (a) and rate performance (b) of a-V_2O_5@C. (a and b) Reproduced with permission.[55] Copyright 2020, Wiley-VCH. Schematic of the process for the preparation of hollow nanotube-like amorphous V_2O_5@C hybrid (c). XRD pattern of an a-V_2O_5@C hybrid (d). (c and d) Reproduced with permission.[56] Copyright 2022, Elsevier. SEM images of C@VO_2@V_2O_5 (e). (e) Reproduced with permission.[57] Copyright 2023, Elsevier. SEM images of the V_2O_5@CNT (f). (f) Reproduced with permission.[58] Copyright 2023, Elsevier. *Ex situ* XRD pattern of N/C@V_2O_3 (g). (g) Reproduced with permission.[59] Copyright 2023, Elsevier. XRD patterns of $Cu_{0.26}V_2O_5$ (h). (h) Reproduced with permission.[60] Copyright 2020, Elsevier.

(VO_2@V_2O_5) interface, as well as the enhanced electron transport efficiency brought by the porous carbon framework, C@VO_2@V_2O_5 exhibited reversible electrochemical reactions and excellent rate capability. This work demonstrates that MOF-derived heterostructure materials are potential cathodes for highly cyclically stable AZIBs. In addition, Liu *et al.* also prepared a V-MOF@CNT-derived V_2O_5@CNT composite, which showed an excellent electrochemical performance by virtue of its unique nanorod composite structure (Fig. 8f),[58] abundant electrochemical active sites and synergistic effect. Zhang *et al.* synthesized a metal–organic framework V-MOF precursor *via* the hydrothermal method, and then synthesized carbon composite vanadium oxide (N/C@V_2O_3) *via* vacuum calcination.[59] *Ex situ* XRD characterization revealed that the electrode material underwent an *in situ* phase transition process during the first charging process, in which the corundum-structured N/C@V_2O_3 was oxidized and transformed into layered alkaline zinc vanadate (N/C@$Zn_2(OH)_3(VO_3)$) (Fig. 8g). This layered structure helped to achieve fast and stable storage and transport of zinc ions. To address the slow kinetics of zinc ion intercalation/deintercalation and poor electrical conductivity of vanadium oxide, Wang *et al.* prepared Cu-MOF-derived Cu-doped V_2O_5 and hierarchical porous carbon ($Cu_{0.26}V_2O_5$@C) composites as cathodes for AZIBs through a direct impregnation and conversion strategy (Fig. 8h).[60] The carbon matrix may improve the electronic conductivity of the material given that its graded porosity may increase the contact between the active material and the electrolyte to achieve efficient penetration of the electrolyte into the material. Thus, the $Cu_{0.26}V_2O_5$@C composite exhibited an excellent cycle life. According to the above-mentioned studies, it can be found that MOF-derived carbon materials can effectively increase the conductivity and maintain their structural stability. Meanwhile, the method for the formation of MOF-derived composites is simple and effective without environmental pollution, which can provide a reference for the preparation of new high-performance cathode materials in the future.

3.6. MOF derivative/Manganese-based materials

To improve the cycle life of manganese-based cathode materials at high current, Sun *et al.* prepared a novel highly

reversible manganese-based cathode material (MnO_x@N–C) with a porous framework and nitrogen doping *via* a metal–organic framework templating method.[61] Firstly, the MnO_2 precursors were obtained *via* a simple hydrothermal reaction. Subsequently, ZIF-8 particles were reformed on the surface of polyvinylpyrrolidone (PVP)-modified MnO_2 nanorods *via* a solvothermal reaction. Finally, nitrogen-doped carbon-coated MnO_x nanorods (MnO_x@N–C) were obtained by thermal treatment (Fig. 9a). Due to this unique porous structure, conductive carbon network (Fig. 9b), and the synergistic effect of Zn^{2+} and Mn^{2+} in the electrolyte, MnO_x@N–C exhibited excellent cycling stability and high reversibility (Fig. 9c). Subsequently, Yin *et al.* also prepared a new coordinatively unsaturated manganese-based metal–organic framework (MOF) as an advanced cathode for AZIBs.[62] Its proper unsaturated coordination degree improved Zn^{2+} transport and electron exchange, ensuring high intrinsic activity and fast electrochemical reaction kinetics during repeated charge/discharge. Therefore, this electrode exhibited a high specific capacity and long cycle life due to the above-mentioned advantages (Fig. 9d). It was found by *ex situ* XRD that the $ZnMn_3O_7{\cdot}3H_2O$ phase was formed during the charge–discharge process due to the strong electrostatic interaction between the Zn^{2+} ions and Mn-H3BTC-MOF-4 matrix (Fig. 9e). This phase was electrochemically active for the deintercalation of zinc ions during subsequent discharge/recharge. In addition, Zhang *et al.* prepared an Mn-based metal–organic framework/carbon nanotube (Mn-MOF/CNT) composite as a cathode material for AZIBs *via* the solvothermal method.[63] Due to the high porosity and high electrical conductivity of the MnMOF/CNT composite, and the Mn^{2+} electrolyte additive, the composite exhibited a satisfactory cycle life (maintains approximately 100% of its capacity after 900 cycles at 1000 mA g^{-1}), which provides a new idea for the design of high-performance cathode materials for ZIBs (Fig. 9f and g).

3.7. C/vanadium-based materials

Zhang *et al.* prepared nitrogen-doped carbon/V_2O_3 microfibers *via* an electrospinning and high-temperature carbonization process.[64] V_2O_3 nanoparticles with a tunnel-like three-dimensional crystal structure were uniformly distributed in an N-doped carbon skeleton (Fig. 10a), and these unique struc-

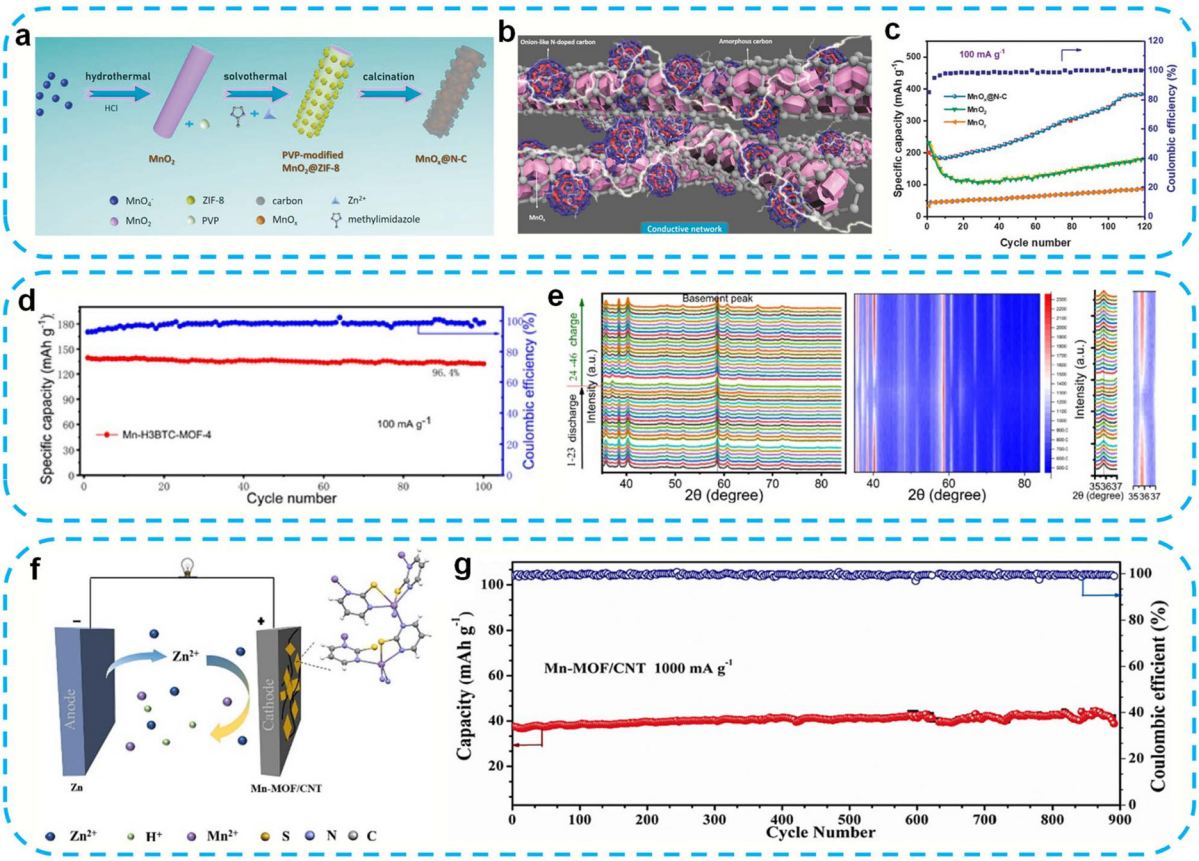

Fig. 9 Schematic of the synthesis of the MnO_x@N–C composite (a). Conductive network between the nanorods (b). Cycling performance of MnO_x@N–C (c). (a–c) Reproduced with permission.[61] Copyright 2018, Wiley-VCH. Cycling performance of Mn-H_3BTC-MOF-4 (d). *Ex situ* XRD patterns of cycled electrodes at different charged/discharged stages (e). (d and e) Reproduced with permission.[62] Copyright 2021, the American Chemical Society. Schematic representation of the Zn//Mn-MOF/CNT (f). Cycling performance of the Mn-MOF/CNT (g). (f and g) Reproduced with permission.[63] Copyright 2024, Elsevier.

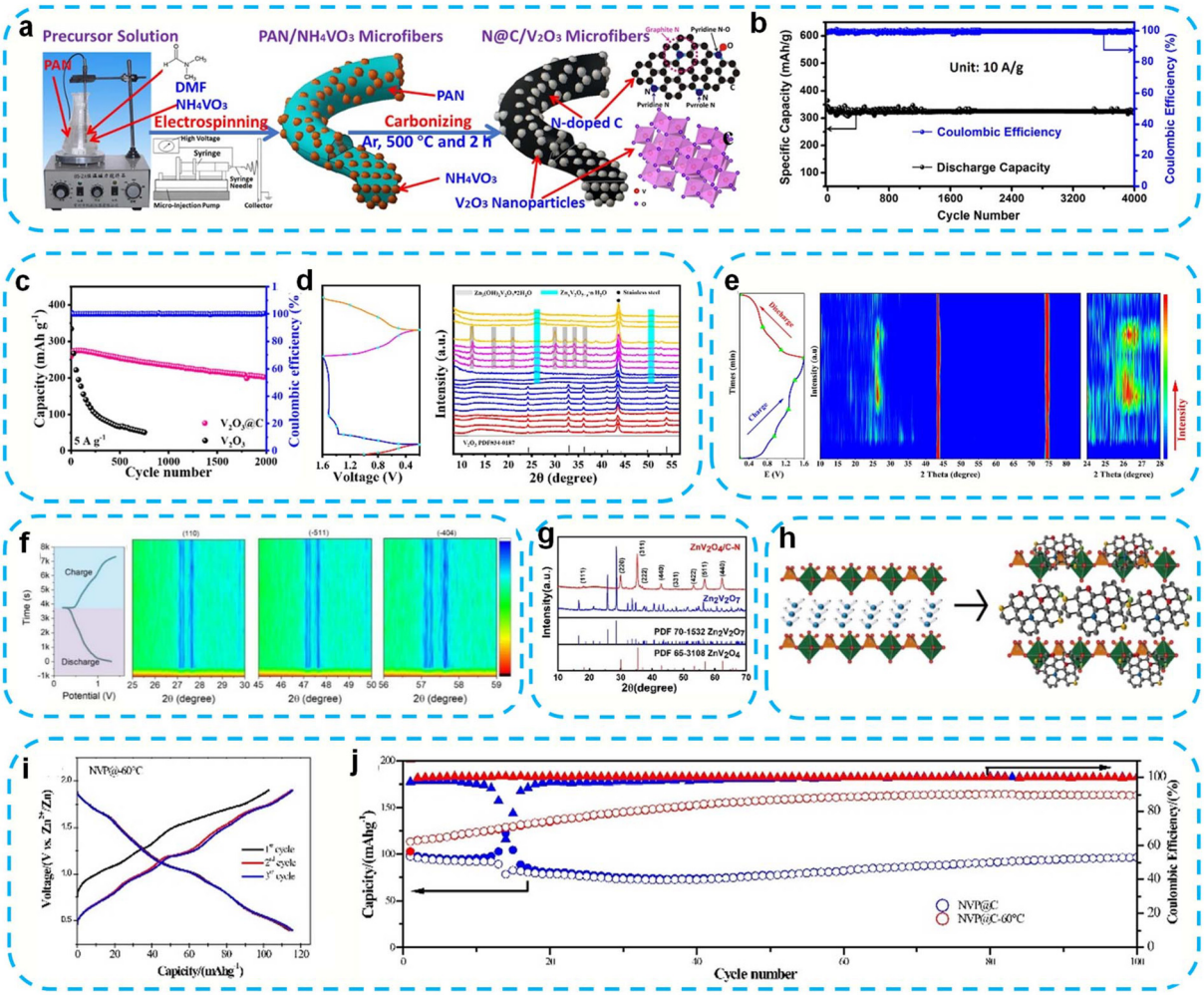

Fig. 10 Schematic of the synthetic process and structure of N@C/V_2O_3 composites (a). Long cycling performance of S-VO85 (b). (a and b) Reproduced with permission.[64] Copyright 2021, Elsevier. Long-term cycling of V_2O_3@C (c). *Ex situ* XRD patterns of V_2O_3@C (d). (c and d) Reproduced with permission.[65] Copyright 2023, the American Chemical Society. *Ex situ* XRD patterns of V_2O_3@CCN-15/2 composites (e). (e) Reproduced with permission.[66] Copyright 2024, Elsevier. High-resolution contour maps of (110), (−511) and (−404) peaks of VO_2@NC (f). (f) Reproduced with permission.[67] Copyright 2022, Elsevier. XRD patterns of $Zn_2V_2O_7$ and ZnV_2O_4/C–N (g). (g) Reproduced with permission.[68] Copyright 2021, Elsevier. Schematic of $VOPO_4$/C (h). (h) Reproduced with permission.[69] Copyright 2022, the American Chemical Society. The charge/discharge profiles of NVP@C-60 °C cathode (i). Cycle performance comparison between NVP@C-60 °C and NVP@C (j). (i and j) Reproduced with permission.[70] Copyright 2023, Elsevier.

tural characteristics enabled the N-doped C/V_2O_3 electrode to maintain a high specific capacity of 322.3 mAh g^{-1} after 4000 cycles at 10 A g^{-1}, and the capacity attenuation in each cycle was only 0.002% (Fig. 10b). Wang *et al.* compounded vanadium oxide and conductive carbon *via in situ* carbonization to improve the conductivity and phase transformation of vanadium-based materials,[65] which significantly improved the performance of the cathode materials (Fig. 10c). The zinc ion storage mechanism was revealed by *ex situ* XRD, and it was found that the *in situ* recombination of V_2O_3 and carbon produced a microstructure that promoted the stable phase transition of $Zn_xV_2O_{5-a}{\cdot}nH_2O$ (ZnVOH), which provided higher Zn^{2+} storage activity than the original phase before electrochemical activation (Fig. 10d). In addition, the Zhou group successfully prepared V_2O_3/carbonized chestnut needle (V_2O_3/CCN) composites using simple evaporation-induced self-assembly technology.[66] The introduction of biomass-derived carbon not only provided a channel to ensure fast electron/ion transmission, but also effectively enhanced the structural stability and conductivity of V_2O_3, and thus the composite material showed an excellent electrochemical performance. *Ex situ* XRD also revealed that the formation of the VO_2 phase during the charge–discharge process and the change in the diffraction peaks during the two charge–discharge processes were similar, which proved the stability of the structure (Fig. 10e). Pang's group reported the simple calcination of ultrathin V_6O_{13} nanobelts coated with polydopamine to prepare a composite of VO_2 and amorphous nitrogen-doped carbon.[67] The amorphous structure of N-doped carbon endowed the layered VO_2@N-doped carbon composite material

with more active sites and higher conductivity. At the same time, the amorphous structure was stable during the ion diffusion process. Therefore, the capacity retention of the VO_2@N-doped carbon composites was as high as 96.3% after 100 cycles at a current density of 1.0 A g^{-1}. The results of *in situ* XRD showed that no other phases were formed, except for a shift in the diffraction peaks during the process of zinc ion intercalation and deintercalation, which proved the structural stability of the VO_2@NC composite (Fig. 10f). In addition, Li *et al.* prepared nitrogen-doped carbon-coated porous ZnV_2O_4 particles (ZnV_2O_4/C–N composite) *via* pyrolysis.[68] The electrochemical performance of the ZnV_2O_4/C–N porous particles as cathode materials in AZIBs was also studied (Fig. 10g). Due to the porous structure and the coating of nitrogen-doped carbon produced by the pyrolysis process, the activity of the V-based cathode improved, and the kinetic performance of ion diffusion was enhanced, thus ensuring the reversible insertion and extraction of zinc ions. ZnV_2O_4/C–N showed a good electrochemical performance. In addition, layered phosphates have been widely used as cathode materials. However, vanadium oxyphosphate ($VOPO_4$) has low electronic conductivity and dissolution problems, which limit its development. Thus, in an effort to solve these problems, Liu *et al.* prepared $VOPO_4$/C by compounding multifunctional carbon materials with the interlayer and outer surface of $VOPO_4$ (Fig. 10h),[69] which not only improved the electronic conductivity of the composite, but also effectively inhibited the dissolution of $VOPO_4$ in the electrolyte. Therefore, this composite material exhibited an excellent rate capability. Alternatively, $Na_3V_2(PO_4)_3$ with a NASICON structure has attracted significant attention due to its three-dimensional ion diffusion channel, high discharge plateau and small volume expansion, and has become a potential cathode material for AZIBs. Lei *et al.* prepared an $Na_3V_2(PO_4)_3$@C composite and cycled the NVP@C cell only once at 60 °C to generate the NVP@C-60 °C composite, which showed an excellent zinc storage performance (Fig. 10i and j).[70]

3.8. C/manganese-based materials

Li *et al.* synthesized MnO@C composites *via* the hydrothermal method and induced the formation of a solid electrolyte interphase, $(Zn(OH)_2)_3(ZnSO_4)(H_2O)_5$ nanosheets,[71] *via in situ* electrochemistry, which covered the surface of MnO@C and effectively prevented direct contact between the electrolyte and the electrode. Thereby, this suppressed the problems of excessive discharge and rapid dissolution of manganese oxides (Fig. 11a). Fig. 11b shows the close contact among the Mn_2O_3, Mn_3O_4 and $(Zn(OH)_2)_3(ZnSO_4)(H_2O)_5$ layers generated during discharge. As a result, MnO@C showed an extremely excellent cycle performance and high specific capacity without adding Mn^{2+} to the electrolyte (Fig. 11c). In addition, Liu's group synthesized a hierarchical accordion-like manganese oxide@carbon (MnO@C) hybrid with strong interaction heterointerfaces *via* the solvothermal method and subsequent calcination (Fig. 11d).[72] The unique hierarchical accordion-like layered structure coupled with the strong interaction heterointerface between the small MnO and carbon matrix effectively improved the ion/electron transfer process and enhanced the structural stability of the MnO@C hybrid materials. This unique structural advantage enabled the MnO@C hybrid to exhibit excellent cycle stability (Fig. 11e). The mechanisms of zinc ion and proton intercalation and deintercalation were also revealed by *ex situ* XRD (Fig. 11f). Zhao *et al.* first annealed $MnCO_3$ at 350 °C to obtain ε-MnO_2, and then coated ε-MnO_2 with a carbon layer (carbonized D-glucose) to obtain ε-MnO@C (Fig. 11g),[73] which effectively alleviated the dissolution of Mn^{2+} and the side reactions between the electrode and the electrolyte. The specific capacity and rate capability of the ε-MnO_2@C cathode were significantly improved by the composite strategy (Fig. 11h). Xie *et al.* also synthesized graphitic carbon-coated δ-MnO_2 nanoparticles *via* a redox route,[74] whose δ-MnO_2 has a two-dimensional layered structure, which allowed the reversible intercalation and deintercalation of metal ions (Fig. 11i). The GC-δ-MnO_2-2 sample delivered a reversible capacity of 277.2 mAh g^{-1} after 100 cycles at 0.3 A g^{-1}, demonstrating its excellent electrochemical performance (Fig. 11j). Yu's group prepared a free-standing cathode with a hierarchical core–shell structure (denoted as MnO_2@NC) by combining layered MnO_2 with N-doped carbon nanowires.[75] Benefiting from the N-doped carbon and rational structure, the MnO_2@NC electrode showed an enhanced rate capability (Fig. 11k). *Ex situ* XRD revealed that $ZnMn_2O_4$ and $Zn_4SO_4(OH)_6{\cdot}4H_2O$ phases were formed with the intercalation and deintercalation of zinc ions and protons during the discharge process, which gradually disappeared during the charge process (Fig. 11l), showing high reversibility. In addition, biomass carbon is also a potential composite matrix. For example, Luo *et al.* found that δ-MnO_2 nanorods grown *in situ* on nitrogen-doped hollow carbon fibers (HCF) derived from natural *Luffa* sponge can significantly improve the ion/electron transfer rate and provide structural stability (Fig. 11m).[76] Density functional theory (DFT) further revealed that the total density of states (TDOS) of HCM is more continuous near the Fermi energy, indicating that HCM has higher intrinsic conductivity (Fig. 11n). Also, the energy barrier for Zn ions to diffuse between the δ-MnO_2 layers was reduced (Fig. 11o). As a result, the HCM electrode still had a capacity retention of 87% after 3500 cycles at 2 A g^{-1}. According to the above-mentioned studies, it can be found that the electrochemical performance can be effectively improved by compounding with C.

3.9. MXene/vanadium-based materials

MXene materials show unique advantages as cathodes for AZIBs due to their diverse structures, high conductivity, rich surface terminal groups, fast ion diffusion kinetics and good mechanical properties. The two-dimensional layered structure and high conductivity of MXenes can be used as a conductive substrate to be composited with manganese and vanadium-based materials to stabilize their structure and improve their conductivity, thereby improving the cycling performance and rate capability of the composites.[77] Furthermore, MXenes have excellent mechanical flexibility, which makes it possible to

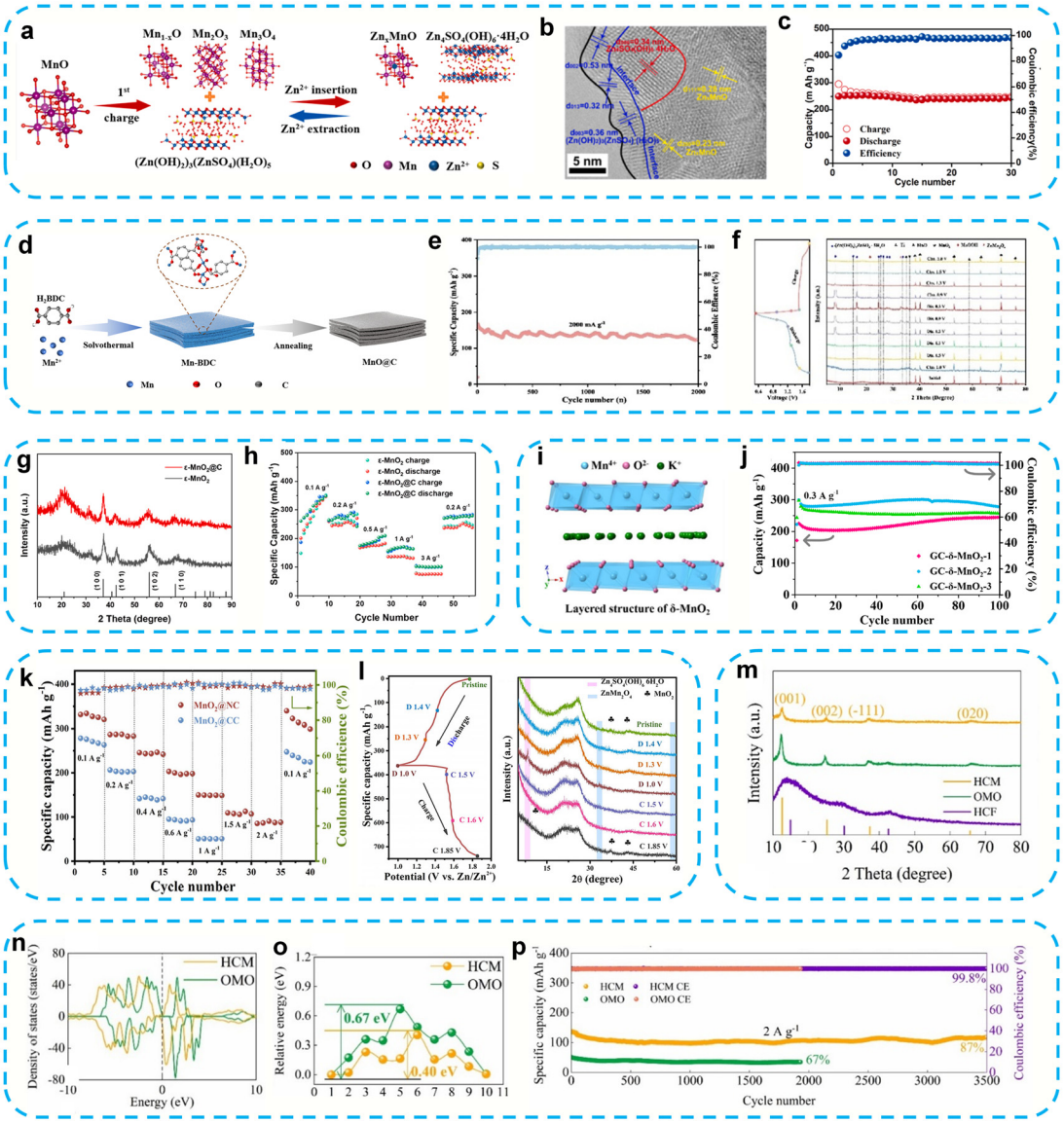

Fig. 11 Crystal structure evolution of the intermediates in the charging–discharging process (a). HRTEM image of MnO@C initially discharged to 0.8 V (b). Cycle performance of MnO@C at 0.1 A g^{-1} (c). (a–c) Reproduced with permission.[71] Copyright 2022, Elsevier. Process for the preparation of the hierarchical accordion-like MnO@C hybrid (d). Long-term cycling stability (e). *Ex situ* XRD patterns of the MnO@C cathode (f). (d–f) Reproduced with permission.[72] Copyright 2022, Elsevier. XRD pattern of ε-MnO_2@C (g). Rate performance of ε-MnO_2@C (h). (g and h) Reproduced with permission.[73] Copyright 2022, Elsevier. Crystalline framework of layered δ-MnO_2 (i). Cycling performance of layered δ-MnO_2 (j). (i and j) Reproduced with permission.[74] Copyright 2022, Springer. Rate performance of MnO_2@NC (k). GCD curves at a current density of 0.2 A g^{-1} and *ex situ* XRD patterns of MnO_2@NC (l). (k and l) Reproduced with permission.[75] Copyright 2023, Wiley-VCH. XRD pattern of HCM (m). TDOS of HCM (n). Diffusion energy barriers of Zn ions in HCM (o). Cycling stability of HCM at 2 A g^{-1} (p). (m–p) Reproduced with permission.[76] Copyright 2023, Elsevier.

manufacture flexible and wearable AZIBs. At present, three main types of MXene materials are used as AZIB cathodes, $Ti_3C_2T_x$, V_2CT_x and Nb_2CT_x. For example, Qin's group reported a method to synthesize vanadium-based oxides on two-dimensional (2D) vanadium carbide MXene (V_2O_x@V_2CT_x), which can be used as an effective cathode material for AZIBs (Fig. 12a).[77] The prepared V_2O_x@V_2CT_x composite exhibited an ideal rate capability, and its average reversible capacity was 304–84 mAh g^{-1} in the current density range of 0.05–2 A g^{-1}, respectively (Fig. 12b). *Ex situ* XRD also revealed the mechanism of zinc ion deintercalation and phase transition (Fig. 12c). In addition, Liu's team self-assembled $Ti_3C_2T_x$ MXene on the surface of V_2O_5 nanoplates through van der Waals force to inhibit the dissolution of vanadium,[78] thereby enhancing the electrochemical zinc storage performance of V_2O_5. In this work, $Ti_3C_2T_x$ MXene, as the interface layer of V_2O_5, can maintain the structural integrity of the cathode material during cycling and inhibit the dissolution of

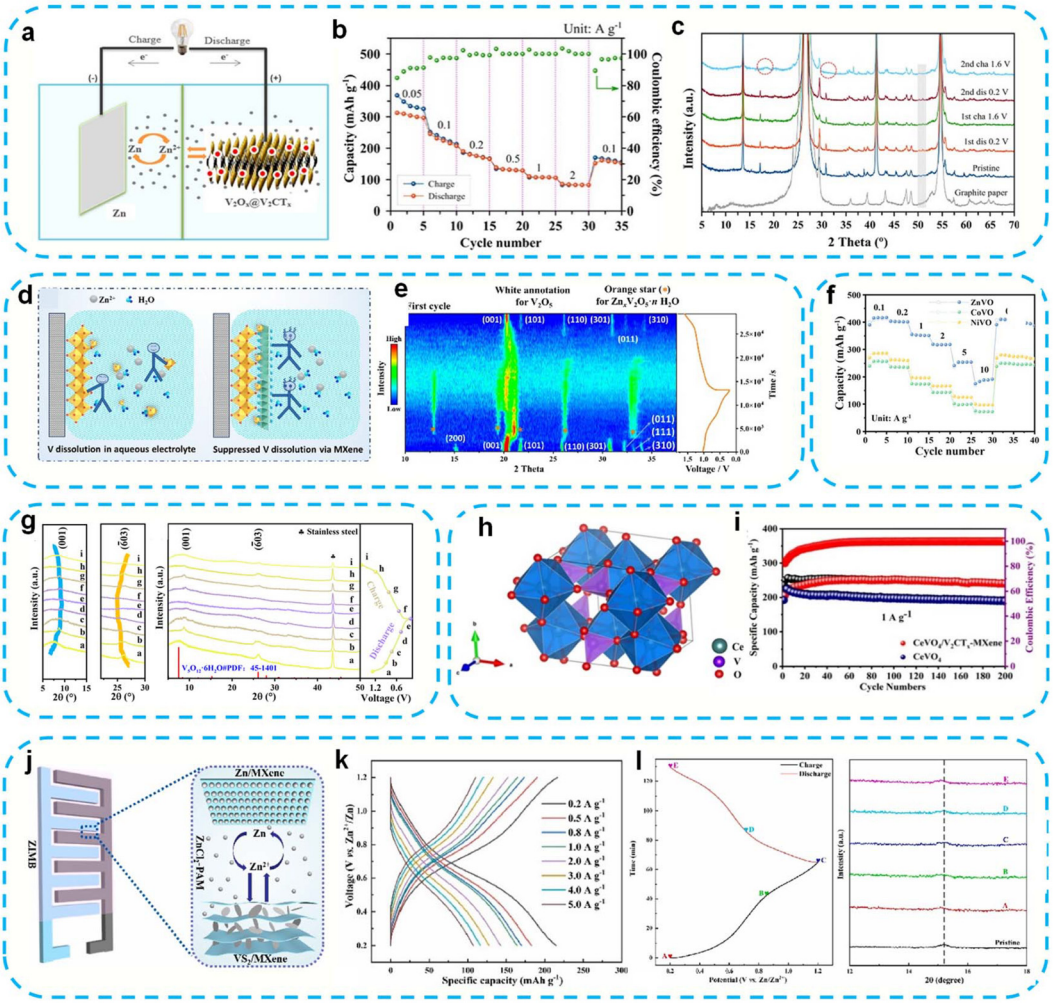

Fig. 12 Schematic of the Zn//V_2O_x@V_2CT_x MXene battery (a). Rate capability of V_2O_x@V_2CT_x MXenes (b). *Ex situ* XRD patterns of V_2CT_x (c). (a–c) Reproduced with permission.[77] Copyright 2020, the American Chemical Society. Illustration of V dissolution in the aqueous electrolyte of V_2O_5 nanoplates and V_2O_5 nanoplate/MXene hybrid cathodes (d). *In situ* XRD characterization of the zinc storage behavior of the VPMX73 cathode (e). (d and e) Reproduced with permission.[78] Copyright 2022, the American Chemical Society. Rate performance of MVO (f). *Ex situ* XRD patterns of ZnVO (g). (f and g) Reproduced with permission.[79] Copyright 2024, the Royal Society of Chemistry. Crystal structure of zircon-type $CeVO_4$ (h). Cycling performance of $CeVO_4$/V_2CT_x-MXenes (i). (h and i) Reproduced with permission.[80] Copyright 2024, Springer. Structure and working mechanism of AZIBs using VS_2/MXenes as the cathode and Zn/MXenes as the anode (j). GCD curves of the optimal VS_2/MXene electrode (k). *Ex situ* XRD patterns at different voltage states (l). (j-l) Reproduced with permission.[81] Copyright 2022, Elsevier.

vanadium. It can be seen from the electrode immersion experiment in Fig. 12d that the stability of the V_2O_5/MXene electrode in the electrolyte was significantly improved compared to the pure V_2O_5 electrode. The *in situ* XRD results (Fig. 12e) demonstrate that the MXene interfacial layer can promote the reversible co-intercalation/deintercalation of water molecules and zinc ions in the V_2O_5/MXene electrode, which weakens the electrostatic repulsion between the host layers, thus facilitating the diffusion of zinc ions. To improve the stability of vanadium-based materials and accelerate the reaction kinetics, Xiao *et al.* successfully prepared three vanadium oxide materials ($M_xV_5O_{12}$, M = Zn^{2+}, Co^{2+}, Ni^{2+}) with V_4C_3 MXene pre-intercalated cations *via* a one-step hydrothermal method.[79] Due to the large interlayer spacing generated by the pre-intercalated Zn^{2+}, the diffusion of ions in the interlayer channel was promoted, and an excellent rate performance is obtained (Fig. 12f). The *ex situ* XRD results demonstrated that Zn^{2+} was successfully pre-intercalated into the structure. Meanwhile, Zn^{2+} has high electronegativity, a large hydrated ionic radius, and strong electron attraction ability and low binding energy with interlayer V–O groups, which contributed to the formation of a stable interlayer structure and large interlayer spacing to ensure the rapid (de) intercalation behavior of Zn^{2+} (Fig. 12g). To improve the performance of vanadium oxides in AZIBs, Xu *et al.* prepared a scaffolded hierarchical $CeVO_4$/V_2CT_x-MXene composite.[80] Fig. 12h shows the crystal structure of $CeVO_4$ with lattice parameters a = 7.400, b = 7.400, c = 6.497, and $\alpha = \beta = \gamma = 90°$. It belongs to the zircon type (space group

$I4_1/amd$) and consists of edge-sharing chains of CeO_8 dodecahedra and VO_4 tetrahedra. Benefiting from the high electron-ion conductivity of V_2CT_x-MXene and the multilayer structure of the composite, the $CeVO_4/V_2CT_x$-MXene cathode exhibited the advantages of zinc storage and ion reaction kinetics. Compared with pure $CeVO_4$, the $CeVO_4/V_2CT_x$-MXene cathode exhibited a higher reversible discharge capacity (Fig. 12i). Liu's group reported a new cathode material of VS_2/MXene flexible zinc-ion microbattery.[81] Due to the large interlayer spacing and hydrophobic nature of VS_2 and the high metallic conductivity of $Ti_3C_2T_x$ MXene, the ion transfer and electron diffusion kinetics in VS_2/MXene were significantly improved (Fig. 12j). It was proven that the electrode exhibited the maximum specific capacity and excellent rate capability when the mass ratio of VS_2 to MXene was 2 : 3 (Fig. 12k). The high reversibility and structural stability of zinc ion intercalation and deintercalation in VS_2/MXene were also demonstrated by *ex situ* XRD (Fig. 12l). The above-mentioned studies show that MXenes play an important role in improving the conductivity and structural stability of vanadium-based materials.

3.10. MXene/manganese-based materials

To improve the cycle life and energy density of MnO_2, Shi *et al.* developed a novel 3D high-density MXene-MnO_2 composite cathode material through a vapor spray drying strategy,[82] in which MnO_2 nanoparticles were encapsulated in MXene nanosheets, effectively constructing a robust and conductive 3D micro-flower-like structure. This structure facilitated fast ion/electron transfer and ensured high structural stability (Fig. 13a). Fig. 13b illustrates the transition between the γ-MnO_2 phase and the layered birnessite phase. To improve the low rate capability and poor cycling performance of manganese-based materials, Zhu *et al.* synthesized a manganese-vanadium hybrid K-V_2C@MnO_2 cathode through metal-

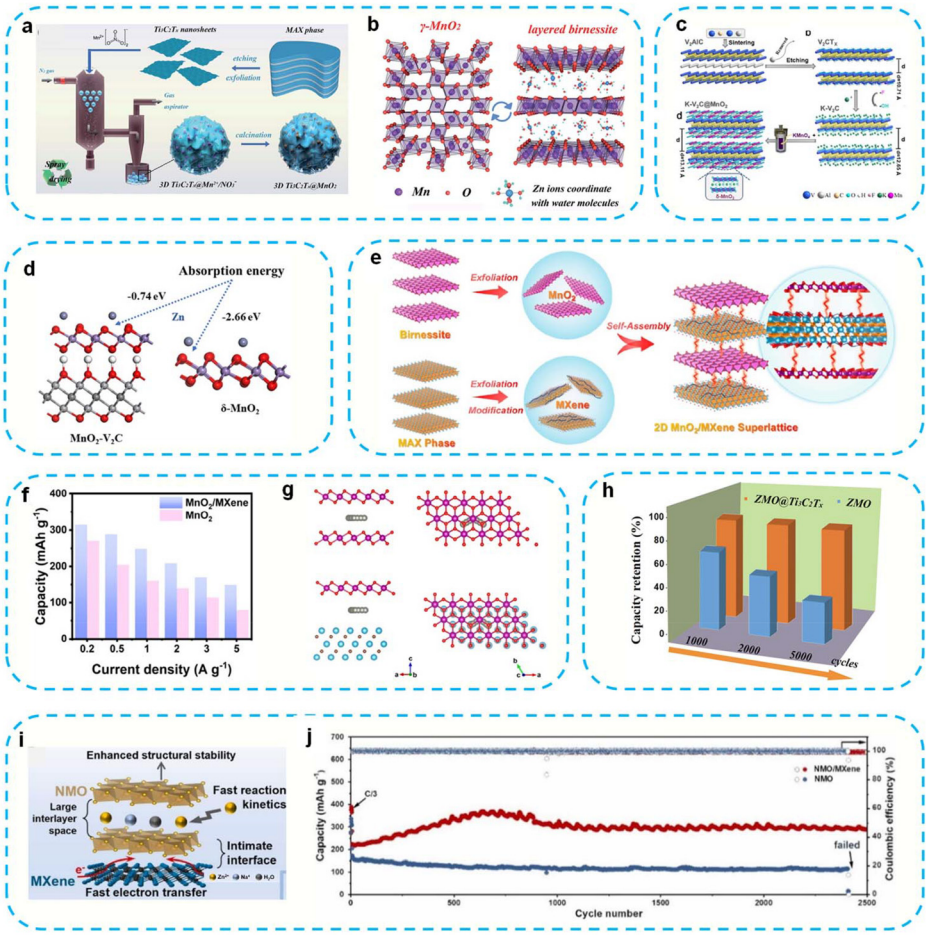

Fig. 13 Schematic of the synthesis process for a 3D $Ti_3C_2T_x$@MnO_2 microflower (a). Schematic of the reversible phase transformation during the charge/discharge process (b). (a and b) Reproduced with permission.[82] Copyright 2020, the Royal Society of Chemistry. Schematic synthesis of K-V_2C@MnO_2 (c). Calculated absorption energies for Zn^{2+} on the surface of perfect MnO_2-V_2C and δ-MnO_2 (d). (c and d) Reproduced with permission.[83] Copyright 2021, the American Chemical Society. Schematic of MnO_2/MXene superlattice synthesis (e). Average capacities of MnO_2 and MnO_2/MXenes (f). Zn^{2+} diffusion paths in MnO_2 and MnO_2/MXenes (g). (e–g) Reproduced with permission.[84] Copyright 2023, the American Chemical Society. Comparison of the capacity retention of pure ZMO and ZMO@$Ti_3C_2T_x$ cathodes after multiple cycles (h). (h) Reproduced with permission.[85] Copyright 2020, Elsevier. Schematic of the structural features of the NMO/MXene cathode (i). Long-term cycling stability of the NMO and NMO/MXene electrodes (j). (i and j) Reproduced with permission.[86] Copyright 2023, Elsevier.

cation interactions (Fig. 13c).[83] The K-V_2C@MnO_2 composite exhibited an excellent electrochemical performance in AZIBs due to the synergistic effects of high conductivity, abundant active sites, Mn^{2+} electrodeposition, and inhibition of MnO_2 structural destruction. According to DFT calculations, the H atom on the –OH functional group of V_2C tends to combine with the O atom of δ-MnO_2, which will help to strengthen the binding force between MnO_2 and the –OH surface of K-V_2C. In addition, the substrate of V_2C affects the adsorption of Zn^{2+} on δ-MnO_2. DFT calculations show that the Gibbs free energy of Zn^{2+} adsorption on MnO_2-V_2C is close to the thermal neutral value (about 0.74 eV), which is significantly lower than that of a Zn ion on the pristine δ-MnO_2 (about 2.66 eV). This result indicates that the thermodynamic adsorption/desorption of

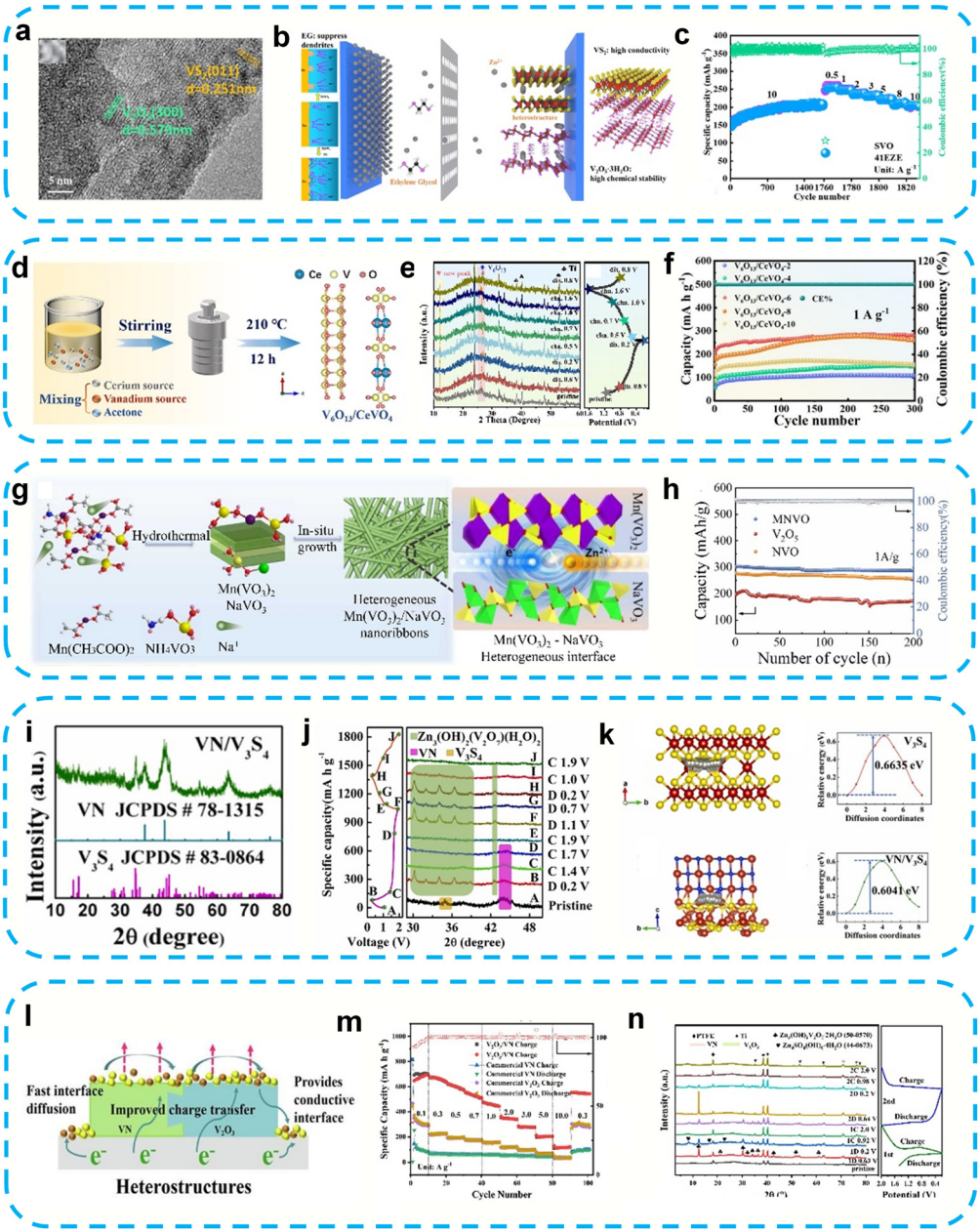

Fig. 14 TEM image of SVO (a). Illustration of the charge/discharge process for the obtained aqueous ZIB (b). Rate capability of SVO (c). (a–c) Reproduced with permission.[87] Copyright 2022, the American Chemical Society. Schematic of the synthesis of V_6O_{13}/$CeVO_4$ (d). *Ex situ* XRD characterization and the corresponding GCD profiles (e). Cycling performance of V_6O_{13}/$CeVO_4$ at 1 A g^{-1} (f). (d–f) Reproduced with permission.[88] Copyright 2023, Elsevier. Preparation and morphology of heterogeneous MNVO (g). Cycling performance at 1 A g^{-1} (h). (g and h) Reproduced with permission.[89] Copyright 2024, Elsevier. XRD pattern of VN/V_3S_4 (i). *Ex situ* XRD results for the O-VN/V_3S_4 cathode (j). Zn^{2+} diffusion pathway and Zn^{2+} diffusion energy barrier curve in V_3S_4 and VN/V_3S_4 (k). (i–k) Reproduced with permission.[90] Copyright 2023, Elsevier. V_2O_3-VN nano-heterojunction electrode zinc storage mechanism (l). Rate performance of the V_2O_3-VN nano-heterojunction (m). Zinc storage mechanism of the V_2O_3-VN nano-heterojunction electrode (n). (l–n) Reproduced with permission.[91] Copyright 2024, Elsevier.

Zn-ions on K-V_2C@ MnO_2 is more reversible than that on δ-MnO_2 (Fig. 13d). Wang *et al.* fabricated 2D MnO_2/MXene superlattices *via* the solution phase assembly of monolayer MnO_2 and $Ti_3C_2T_x$ MXene nanosheets,[84] in which the monolayer MnO_2 nanosheets were separated and stabilized between the monolayer MXene nanosheets (Fig. 13e). MXene nanosheets can not only be used as a structural stabilizer to isolate MnO_2 nanosheets and prevent their aggregation, but also enhance their conductivity, thus maintaining the stability of the overall structure and achieving fast electron transport. Therefore, compared with MnO_2, MnO_2/MXene exhibited a better rate performance (Fig. 13f). Theoretical calculations also revealed that the ion diffusion energy barrier in MnO_2/MXene is much lower than that in MnO_2 (Fig. 13g), confirming the performance of ultrafast H^+ and Zn^{2+} transport in MnO_2/MXene. To suppress the irreversible reaction during zinc storage in $ZnMn_2O_4$ (ZMO), Shi *et al.* synthesized a 3D assembly of Ti-MXene ($Ti_3C_2T_x$)-stabilized ZMO nanoparticles.[85] Therefore, the ZMO@$Ti_3C_2T_x$ composite cathode exhibited a high reversible specific capacity and excellent rate capability (Fig. 13h). In addition, to further improve the rate capability and energy density of manganese-based materials, Liu *et al.* also successfully proposed a pre-intercalated manganese oxide ($Na_{0.55}Mn_2O_4{\cdot}1.5H_2O$)/MXene hybrid material (NMO/MXene).[86] The synergistic interaction between MXene and NMO greatly improved the structural stability of NMO and promoted fast charge transfer and the ion diffusion kinetics (Fig. 13i). Therefore, the as-prepared NMO/MXene cathode achieved a long cycle life of more than 2500 cycles at 5 C (Fig. 13j). The above-mentioned studies demonstrate that the MXene-mediated advanced manganese-based cathode strategy opens up a new way to construct high-performance zinc-ion batteries.

3.11. Other compounds/vanadium-based materials

Gao *et al.* proposed a dual-phase $V_2O_5{\cdot}3H_2O$@VS_2 (SVO) nanocomposite cathode material for high-efficiency zinc-ion batteries by combining the high conductivity of vanadium sulfide with the high chemical stability of vanadium oxide.[87] The biphasic features of VS_2 and $V_2O_5{\cdot}3H_2O$ can be seen from the high-resolution TEM (HRTEM) image in Fig. 14a. The charge–discharge mechanism of zinc ions is also shown in Fig. 14b. The electrochemical synergy between $V_2O_5{\cdot}3H_2O$ and VS_2 endowed the SVO composite with a high reversible capacity and stable cycling performance. Because the structural water in $V_2O_5{\cdot}3H_2O$ can be used as a shielding layer to weaken the electrostatic interaction, and VS_2 can enhance the conductivity, this composite exhibited a high specific capacity (Fig. 14c). To improve the Zn^{2+} diffusion rate and cycling stability in V-based materials, Cheng *et al.* synthesized nanosheet V_6O_{13}/$CeVO_4$ composites *via* a one-step hydrothermal method (Fig. 14d).[88] The storage mechanism of zinc ions was also studied by *ex situ* XRD, and the results revealed the high reversibility of the V_6O_{13}/$CeVO_4$ electrode material (Fig. 14e). The synergistic effect of V_6O_{13} and $CeVO_4$ effectively accelerated the transfer of zinc ions, and thus V_6O_{13}/$CeVO_4$-6 exhibited a high capacity and excellent cycle life (Fig. 14f). In addition, to further improve the slow kinetics and structural stability of V-based materials, Lu *et al.* prepared a heterogeneous $Mn(VO_3)_2$/$NaVO_3$ (MnVO) nanoribbon hybrid as a high-performance cathode for zinc storage *via* the hydrothermal method (Fig. 14g).[89] The Mn$(VO_3)_2$/$NaVO_3$(MnVO) nanoribbons exhibited a high specific capacity and long cycle stability (Fig. 14h) due to the heterointerface between $Mn(VO_3)_2$ and $NaVO_3$, which facilitated the charge transfer kinetics and led to enhanced zinc diffusion kinetics. Because of its metal-like properties, VN is often compounded with other compounds to enhance their conductivity. For example, Chen's group also prepared a heterostructure composite material (VN/V_3S_4) composed of vanadium nitride and V_3S_4 (Fig. 14i).[90] The transformation mechanism of the heterogeneous vanadium redox reaction with the intercalation and deintercalation of Zn^{2+} in the first cycle was revealed by *ex situ* XRD (Fig. 14j). In addition, the Zn^{2+} diffusion barrier was calculated by density functional theory. Compared with V_3S_4, VN/V_3S_4 has a lower diffusion energy barrier, which means a smoother zinc ion insertion/extraction process, thus significantly enhancing the electrochemical energy storage capacity of VN/V_3S_4 (Fig. 14k). In addition, Wu *et al.* also prepared V_2O_3-VN heterojunction composites with an urchin-like morphology as cathodes for AZIBs.[91] The V_2O_3-VN composite material was composed of different crystal planes of V_2O_3 and VN, and an effective heterointerface network (Fig. 14l) was formed in the bulk electrode, which is the reason for its good electrochemical performance (Fig. 14m). *Ex situ* XRD revealed that the V_2O_3-VN heterojunction underwent a phase transition during the first charge–discharge process, resulting in the formation of the $Zn_3(OH)_2V_2O_7{\cdot}2H_2O$ electrode, and a reversible redox reaction from V^{4+} to V^{5+} also occurred during the second charge–discharge process (Fig. 14n).

4. Summary and outlook

Because of their high theoretical capacity, high safety, abundant zinc resources and environmental friendliness, AZIBs have become a research hotspot in the field of energy storage. As an important part of AZIBs, the performance of cathode materials directly affects the overall performance of the battery. Therefore, it is urgent to explore high-performance cathode materials for AZIBs. At present, to improve the electrochemical performance of cathode materials, researchers have adopted many strategies, including doping, compounding, crystallization, and introducing defect structures. Herein, a large number of current research methods for improving the electrochemical performance by compositing, as well as related synthesis strategies and electrochemical zinc storage mechanisms, were reviewed, aiming to provide a reference for the development of high-performance cathode materials for AZIBs and promote the improvement of AZIBs in practical applications. According to the current research status, to further break through the comprehensive performance of AZIBs, further exploration is needed from the following perspectives in the future.

4.1. Developing a high-entropy strategy

By incorporating four to five environmentally friendly metal elements (*e.g.*, titanium, iron, and cobalt) into vanadium-based/manganese-based frameworks, a high-entropy material system is constructed, leveraging lattice distortion effects and synergistic modulation of the electronic structures among multiple elements to achieve the simultaneous enhancement of ionic conductivity and structural stability. The multi-component nature of high-entropy materials facilitates their integration with green synthesis methods such as low-temperature solvothermal processes and microwave-assisted synthesis, significantly reducing the energy consumption and use of hazardous reagents. Furthermore, multi-element doping broadens the electronic band structure, creating efficient ion diffusion pathways, while enhancing corrosion resistance and thermal stability, thereby enabling applications in extreme environments. This high-entropy strategy transcends the limitations of traditional single-component material designs by establishing an intrinsically safe material system through elemental diversity, offering a novel paradigm for the development of recyclable, low-environmental-impact AZIBs. Although not yet widely explored in Zn-ion cathodes, high-entropy materials represent a promising extension of composite design principles for multi-elemental stabilization.

4.2. Defect-composite coupling

Future research necessitates the integration of cross-scale modeling approaches, including first-principles calculations, molecular dynamics, and phase-field simulations to quantitatively elucidate the dynamic interplay between defects (*e.g.*, vacancies, dislocations, and grain boundaries) and composite interfaces/reinforcing phases, particularly under extreme conditions (elevated temperatures, irradiation, and high-stress fields). Concurrently, the development of *in situ* characterization techniques with high spatiotemporal resolution, such as *in situ* transmission electron microscopy coupled with deep learning-based image analysis and synchrotron radiation-based 3D imaging is essential to capture, in real-time, the nucleation, migration, and interfacial reaction processes of defects within composites, thereby providing direct experimental validation for theoretical models. Also, artificial intelligence (AI)-driven defect design strategies need to be explored to optimize the type, density, and spatial distribution of defects within composite materials *via* machine learning (ML). This approach aims to achieve directional coupling among defects, interfaces, and reinforcing phases, thereby enabling the proactive tailoring of material properties. Concurrently, the design of intelligent interfacial layers featuring gradient or hierarchical architectures is critical. Leveraging their chemical/mechanical coupling effects with defects will facilitate the development of next-generation high-performance composites.

4. 3. Developing low-energy manufacturing

Developing low-energy techniques is essential to realize the scalable and controlled fabrication of composites, ultimately facilitating the translation of laboratory findings into industrial applications. The transition to sustainable composite manufacturing requires breakthrough low-energy technologies. Future research should explore non-thermal processing platforms, such as plasma-enhanced atomic assembly, flash Joule heating, enzyme-catalyzed room-temperature synthesis and cold sintering, to construct multi-scale interfaces at low temperatures instead of high-energy thermal processing. At the same time, digital twin technology driven by artificial intelligence should be used to reduce energy consumption by dynamically optimizing the phase distribution and defect topology through machine learning. To realize the closed-loop of the whole life cycle of materials, the scale of the low-carbon cycle should be expanded, including room temperature dissolution regeneration and direct waste upgrading, and renewable energy should be used as power. Based on the premise of maintaining high resource utilization efficiency, the regeneration of high-performance composite materials is realized (Fig. 15).

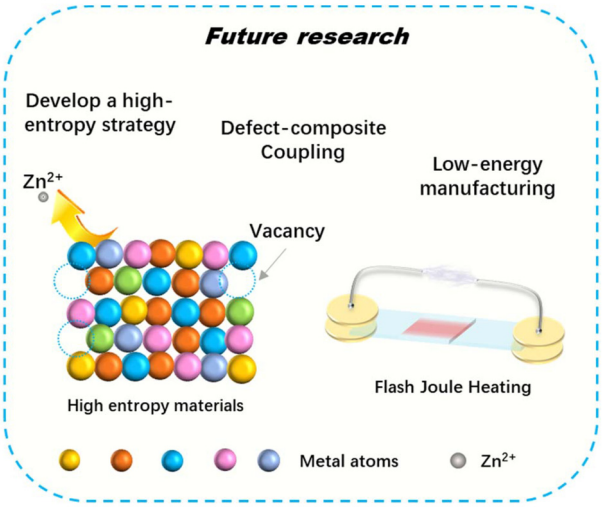

Fig. 15 Illustration of future research directions.

In summary, compositing is an effective strategy to improve the performance of electrode materials, but the development of high-performance cathode materials still faces many challenges at this stage. We believe that this review can provide a comprehensive overview of this strategy and propose modification suggestions, hoping to provide some reference value for the preparation of new high-performance materials.

Author contributions

Tao Song designed the framework of the review and wrote the review. Weifeng Fan looked up most of the papers and proposed some suggestions. Yu Hu provided the methodology for the review. Heng Zhang and Youcun Bai conceived the project as well as supervised and discussed the review.

Conflicts of interest

The authors declare no conflict of interest.

Data availability

No primary research results, software or code has been included and no new data were generated or analysed as part of this review.

Acknowledgements

This work is funded by the Natural Science Foundation of Jiangsu Province (BK20240999) and Natural Science Research Project of Higher Education Institutions in Jiangsu Province (24KJB430040).

References

1 H. Y. Lu, J. S. Hu, X. J. Wei, K. Q. Zhang, X. Xiao, J. X. Zhao, Q. Hu, J. Yu, G. M. Zhou and B. G. Xu, *Nat. Commun.*, 2023, **14**, 4435.
2 F. H. Cui, R. Pan, L. Su, C. Y. Zhu, H. Z. Lin, R. Q. Lian, R. N. Fu, G. J. Zhang, Z. J. Jiang, X. C. Hu, Y. C. Pan, S. S. Hou, F. C. Zhang, K. Zhu, Y. H. Dong and F. Xu, *Adv. Mater.*, 2023, **35.**, 2306580.
3 Y. X. Tong, S. D. Su, X. M. Li, B. Liang, J. Peng, J. H. Hou and M. Luo, *J. Power Sources*, 2022, **528**, 231226.
4 J. L. Zhang, Q. Wu, S. Yang, F. S. Luo, Y. Li, Y. H. Zhang, K. Chen, J. Huang, H. B. Xie and Y. W. Chen, *Green Chem.*, 2024, **26**, 6723.
5 G. D. Cui, Y. X. Zeng, J. F. Wu, Y. Guo, X. J. Gu and X. W. Lou, *Adv. Sci.*, 2022, **9**, 2106067.
6 X. Y. Chen, A. J. Zhang, H. Zou, L. Li, Q. C. Zhu and W. M. Zhang, *Energy Storage Mater.*, 2024, **70**, 103457.
7 T. Zhou and G. Gao, *Nano Energy*, 2024, **127**, 109691.
8 C. Guo, S. Yi, R. Si, B. J. Xi, X. G. An, J. Liu, J. F. Li and S. L. Xiong, *Adv. Energy Mater.*, 2022, **12**, 2202039.
9 J. Y. Liu, Z. R. Shen and C. Z. Lu, *J. Mater. Chem. A*, 2024, **12**, 2647–2672.
10 Y. X. Zeng, X. F. Lu, S. L. Zhang, D. Y. Luan, S. Li and X. W. Lou, *Angew. Chem., Int. Ed.*, 2021, **60**, 22189–22194.
11 W. Li, X. Y. Jing and K. Jiang, *ACS Appl. Energy Mater.*, 2021, **4**, 2797–2807.
12 M. L. Agiorgousis, Y. Y. Sun, D. West and S. B. Zhang, *ACS Appl. Energy Mater.*, 2018, **1**, 440–446.
13 C. X. Guo, Y. Liu, L. Q. Wang, D. J. Kong and J. M. Wang, *ACS Sustainable Chem. Eng.*, 2022, **10**, 213–223.
14 W. X. Zhao, Y. B. Zhou, H. Zhou, X. Q. Wang, S. J. Sun, X. He, Y. S. Luo, B. W. Ying, Y. C. Yao, X. Q. Ma and X. P. Sun, *Adv. Sci.*, 2025, **12**, 2411884.
15 W. X. Zhao, X. Q. Ma, X. D. Wang, H. Zhou, X. He, Y. C. Yao, Y. C. Ren, Y. S. Luo, D. D. Zheng, S. J. Sun, Q. Liu, L. M. Li, W. Chu, Y. Wang and X. P. Sun, *Small*, 2024, **20**, 2311055.
16 Z. Q. Li, Y. K. Ren, L. Mo, C. F. Liu, K. Hsu, Y. C. Ding, X. X. Zhang, X. L. Li, L. H. Hu, D. H. Ji and G. Z. Cao, *ACS Nano*, 2020, **14**, 5581–5589.
17 J. W. Ding, H. Y. Zheng, H. G. Gao, Q. N. Liu, Z. Hu, L. F. Han, S. W. Wang, S. D. Wu, S. M. Fang and S. L. Chou, *Adv. Energy Mater.*, 2021, **11**, 2100973.
18 Q. Zang, X. J. Cheng, S. J. Chen, Z. Y. Xiao, K. P. Wang, L. B. Zong, Q. Zhang and L. Wang, *Chem. Eng. J.*, 2023, **452**, 139396.
19 Z. Wu, J. Yao, C. Chen, X. Chen, X. X. Pan, J. J. Zheng, Y. Gan, J. Y. Li, X. T. Liu, C. Xia, L. Lv, H. Wang and H. Z. Wan, *Chem. Eng. J.*, 2024, **479**, 147889.
20 L. L. Chen, Z. H. Yang, J. Wu, H. Z. Chen and J. L. Meng, *Electrochim. Acta*, 2020, **330**, 135347.
21 L. L. Wang, Z. X. Wu, M. J. H. Jiang, J. Y. Lu, Q. H. Huang, Y. Zhang, L. J. Fu, M. Wu and Y. P. Wu, *J. Alloys Compd.*, 2020, **8**, 9313–9321.
22 Y. C. Bai, L. Luo, W. L. Song, S. S. Man, H. Zhang and C. M. Li, *Adv. Sci.*, 2024, **11**, 2308668.
23 T. Xiong, Y. X. Zhang, W. S. V. Lee and J. M. Xue, *Adv. Energy Mater.*, 2020, **10**, 2001769.
24 X. W. Cao, Y. T. Xu, B. Yang, H. Z. Lang, Z. X. Shen, N. Wang, X. F. Wang, S. H. Wang and C. L. Sun, *J. Alloys Compd.*, 2022, **896**, 162785.
25 Z. Wang, Y. R. Wang, Y. X. Lin, G. Bian, H. Yang, L. X. Li, J. Yin and J. Zhu, *ACS Appl. Mater. Interfaces*, 2022, **14**, 47725–47736.
26 C. Wang, Y. X. Zeng, X. Xiao, S. J. Wu, G. B. Zhong, K. Q. Xu, Z. F. Wei, W. Su and X. Lu, *J. Energy Chem.*, 2020, **43**, 182–187.
27 L. Zhang, S. H. Yang, W. Q. Fu, Y. W. Cui, J. Q. Wang, D. G. Zhao, C. Yang, X. T. Wang and B. Q. Cao, *J. Mater. Sci. Technol.*, 2022, **127**, 206–213.
28 C. Y. Zhao, M. Q. Wu, W. C. Lu, Y. J. Cheng, X. Y. Zhang, I. Saadoune, R. Q. Lian, Y. Z. Wang and Y. J. Wei, *Small*, 2024, **20**, 2401379.
29 Y. H. Xu, G. N. Zhang, J. Q. Liu, J. H. Zhang, X. X. Wang, X. H. Pu, J. J. Wang, C. Yan, Y. Y. Cao, H. J. Yang, W. B. Li and X. F. Li, *Energy Environ. Mater.*, 2023, **6**, e12575.
30 K. X. Cai, S. H. Luo, J. Feng, J. C. Wang, Y. Zhan, Q. Wang, Y. H. Zhang and X. Liu, *Chem. Rec.*, 2022, **22**, e202100169.
31 H. S. Jia, Z. M. Zhang, S. Q. Li, M. Han, Y. Long, C. B. Liu, Q. S. Wang and W. Q. Liu, *ACS Appl. Nano Mater.*, 2024, **7**, 15387–15394.
32 F. Wan, S. Huang, H. M. Cao and Z. Q. Niu, *ACS Nano*, 2020, **14**, 6752–6760.
33 S. Gull, S. C. Huang, C. S. Ni, S. F. Liu, W. H. Lin and H. Y. Chen, *J. Mater. Chem. A*, 2022, **10**, 14540–14554.
34 G. B. Xu, X. Liu, S. J. Huang, L. Li, X. L. Wei, J. X. Cao, L. W. Yang and P. K. Chu, *ACS Appl. Mater. Interfaces*, 2020, **12**, 706–716.
35 D. W. Rao, W. W. Zhang, B. C. Cheng, Y. Wang, C. S. F. Lei, Q. Y. An, M. Huang and L. Q. Mai, *Batteries Supercaps*, 2024, **7**, e202400046.

36 Y. Ba, H. S. Wang, P. C. Zhang, Z. S. Wen, S. Li and J. C. Sun, *Mater. Lett.*, 2024, **355**, 135523.
37 K. Wang, X. H. Zhang, J. W. Han, X. Zhang, X. Z. Sun, C. Li, W. H. Liu, Q. W. Li and Y. W. Ma, *ACS Appl. Mater. Interfaces*, 2018, **10**, 24573–24582.
38 X. L. Guo, H. Sun, C. G. Li, S. Q. Zhang, Z. H. Li, X. Y. Hou, X. B. Chen, J. Y. Liu, Z. Shi and S. H. Feng, *J. Energy Chem.*, 2022, **68**, 538–547.
39 Z. W. Tong, Y. F. Yuan, D. Zhang, S. M. Yin and S. Y. Guo, *Electrochim. Acta*, 2022, **403**, 139649.
40 Y. T. Yang, T. Shao, Y. Zhang, Y. Y. Lu, M. Li, H. M. Liu, Q. J. Xu and Y. Y. Xia, *J. Power Sources*, 2023, **564**, 232863.
41 X. Wang, Y. G. Li, S. Wang, F. Zhou, P. Das, C. L. Sun, S. H. Zheng and Z. S. Wu, *Adv. Energy Mater.*, 2020, **10**, 2000081.
42 X. Q. Zhong, Z. Z. Kong, Q. F. Liu, C. Yang, Y. Chen, J. H. Qiu and L. M. Zang, *ACS Appl. Mater. Interfaces*, 2023, **15**, 58333–58344.
43 B. X. Lan, C. Tang, L. N. Chen, W. W. Zhang, W. Tang, C. L. Zuo, X. D. Fu, S. J. Dong, Q. Y. An and P. Luo, *J. Alloys Compd.*, 2020, **818**, 153372.
44 T. H. Wu, J. A. Chen, W. S. Lin and W. Y. Liang, *J. Electrochem. Soc.*, 2021, **168**, 080527.
45 Y. S. Cai, F. Liu, Z. G. Luo, G. Z. Fang, J. Zhou, A. Q. Pan and S. Q. Liang, *Energy Storage Mater.*, 2018, **13**, 168–174.
46 S. M. Huang, S. G. He, H. Q. Qin and X. H. Hou, *ACS Appl. Mater. Interfaces*, 2021, **13**, 44379–44388.
47 J. S. Park, S. E. Wang, D. S. Jung, J. K. Lee and Y. C. Kang, *Chem. Eng. J.*, 2022, **446**, 137266.
48 M. Narayanasamy, L. T. Hu, B. Kirubasankara, Z. Liu, S. Angaiahb and C. Yan, *J. Alloys Compd.*, 2021, **882**, 160704.
49 H. G. Qin, Z. H. Yang, L. L. Chen, X. Chen and L. M. Wang, *J. Mater. Chem. A*, 2018, **6**, 23757.
50 C. Y. Wang, M. Q. Wang, Z. C. He, L. Liu and Y. D. Huang, *ACS Appl. Energy Mater.*, 2020, **3**, 1742–1748.
51 J. Y. Chen, J. X. Liang, Y. Zhou, Z. Sha, S. Lim, F. Huang, Z. J. Han, S. A. Brown, A. L. Y. Cao, D. W. Wang and C. H. Wang, *J. Mater. Chem. A*, 2021, **9**, 575.
52 S. X. Ding, M. Z. Zhang, R. Z. Qin, J. J. Fang, H. Y. Ren, H. C. Yi, L. L. Liu, W. G. Zhao, Y. Li, L. Yao, S. N. Li, Q. H. Zhao and F. Pan, *Nano-Micro Lett.*, 2021, **13**, 173.
53 Y. X. Guo, Z. D. Zhao, J. J. Zhang, Y. C. Liu, B. Hu, Y. X. Zhang, Y. H. Ge and H. B. Lu, *Electrochim. Acta*, 2022, **411**, 140045.
54 G. F. Zeng, Q. Sun, Y. Feng, X. X. Wang, X. Y. Ma, J. Li, H. Zhang, S. Wang, I. Y. Wen, J. Y. Feng, L. J. Ci, A. Cabot and Y. H. Tian, *ACS Nano*, 2023, **17**, 13256–13268.
55 S. Deng, Z. Yuan, Z. Tie, C. Wang, L. Song and Z. Niu, *Angew. Chem., Int. Ed.*, 2020, **59**, 22002–22006.
56 C. L. Li, M. Li, H. T. Xu, F. Zhao, S. Q. Gong, H. H. Wang, J. J. Qi, Z. Y. Wang, X. B. Fan, W. C. Peng and J. P. Liu, *J. Colloid Interface Sci.*, 2022, **623**, 277–284.
57 Y. X. Tong, Y. Zhao, M. Luo, S. D. Su, Y. Q. Yang, Y. Zang, X. M. Li, L. F. Wang and J. Z. Fang, *J. Alloys Compd.*, 2023, **932**, 167681.
58 M. M. Liu, Z. H. Li and Y. B. Zhang, *J. Electroanal. Chem.*, 2023, **942**, 117576.
59 M. Zhang, P. F. Wang, X. N. Lv, Y. B. Yang, Y. H. Zhang, Y. H. Wu, L. Zhao, G. Yang and F. N. Shi, *J. Alloys Compd.*, 2023, **960**, 170790.
60 X. W. Wang, B. Zhan, J. M. Feng, L. Q. Wang, B. Wu, J. F. Zhang, X. Ou, F. Hou and J. Liang, *Sustainable Mater. Technol.*, 2020, **26**, e00236.
61 Y. Q. Fu, Q. L. Wei, G. X. Zhang, X. M. Wang, J. H. Zhang, Y. F. Hu, D. N. Wang, L. Zuin, T. Zhou, Y. C. Wu and S. H. Sun, *Adv. Energy Mater.*, 2018, **8**, 1801445.
62 C. J. Yin, C. L. Pan, X. B. Liao, Y. S. Pan and L. Yuan, *ACS Appl. Mater. Interfaces*, 2021, **13**, 35837–35847.
63 J. Zhang, Y. X. Liu, T. T. Wang, N. Fu and Z. L. Yang, *J. Energy Storage*, 2024, **76**, 109873.
64 H. B. Zhang, Z. D. Yao, D. W. Lan, Y. Y. Liu, L. T. Ma and J. L. Cui, *J. Alloys Compd.*, 2021, **861**, 158560.
65 D. Q. Wang, W. H. Liang, X. D. He, Y. Yang, S. Wang, J. Li, J. C. Wang and H. L. Tin, *ACS Appl. Mater. Interfaces*, 2023, **15**, 20876–20884.
66 G. L. Zeng, Y. Q. Wang, X. M. Lou, H. Chen, S. H. Jiang and W. Zhou, *J. Energy Storage*, 2024, **77**, 109859.
67 T. T. Lv, X. Luo, G. Q. Yuan, S. Y. Yang and H. Pang, *Chem. Eng. J.*, 2022, **428**, 131211.
68 S. J. Li, L. P. Qin, L. J. Li, H. Cheng, G. Z. Fang, S. Q. Liang, Q. Zhu and M. M. Chen, *Mater. Today Commun.*, 2021, **27**, 102271.
69 Y. H. Liu, W. H. Li, H. Y. Lü, X. X. Luo, Z. X. Huang, Z. Y. Gu, X. X. Zhao and X. L. Wu, *ACS Appl. Mater. Interfaces*, 2022, **14**, 45494–45502.
70 P. Lei, J. H. Liu, S. Y. Zhuge and Z. Lü, *J. Electroanal. Chem.*, 2023, **928**, 117027.
71 S. Y. Li, D. X. Yu, L. Liu, S. Y. Yao, X. Q. Wang, X. Jin, D. Zhang and F. Du, *Chem. Eng. J.*, 2022, **430**, 132673.
72 C. L. Li, M. Li, H. T. Xu, F. Zhao, S. Q. Gong, H. H. Wang, J. J. Qi, Z. Y. Wang, Y. Q. Hu, W. C. Peng, X. B. Fan and J. P. Liu, *J. Colloid Interface Sci.*, 2022, **628**, 553–561.
73 W. Y. Zhao, Q. Q. Kong, X. Q. Wu, X. G. An, J. Zhang, X. N. Liu and W. T. Yao, *Appl. Surf. Sci.*, 2022, **605**, 154685.
74 Q. X. Xie, L. H. Huang, Z. J. Liang, S. C. Tang, W. Z. Ling, Q. X. Huang, Z. H. Zhou, X. H. Su, T. Xue and G. Cheng, *J. Electron. Mater.*, 2023, **52**, 41–49.
75 X. H. Li, Q. C. Zhou, Z. Yang, X. Zhou, D. Qiu, H. J. Qiu, X. T. Huang and Y. Yu, *Energy Environ. Mater.*, 2023, **6**, e12378.
76 S. J. Luo, J. Xu, B. H. Yuan, L. L. Chen, L. Xu, R. Zheng, Y. S. Wang, M. J. Zhang, Y. Lu and Y. S. Luo, *Carbon*, 2023, **214**, 118334.
77 R. Venkatkarthick, N. Rodthongkum, X. Y. Zhang, S. M. Wang, P. Pattananuwat, Y. S. Zhao, R. P. Liu and J. Q. Qin, *ACS Appl. Energy Mater.*, 2020, **3**, 4677–4689.
78 H. Liu, L. Jiang, B. Cao, H. L. Du, H. Lu, Y. Ma, H. Wang, H. Y. Guo, Q. Z. Huang, B. Xu and S. J. Guo, *ACS Nano*, 2022, **16**, 14539–14548.
79 W. H. Xiao, S. H. Yang, R. Jiang, Q. F. Huang, X. Y. Shi, Y. H. Tsang, L. Y. Shao and Z. P. Sun, *J. Mater. Chem. A*, 2024, **12**, 5530.

80 W. G. Xu, X. N. Zhang, J. H. Li, X. B. Chen, L. Lan, J. Zhang, F. C. C. Ling and Q. Ru, *Ionics*, 2024, **30**, 1457–1467.
81 Y. M. Feng, Y. L. Feng, Y. Zhang, L. L. Sun, X. L. Li, M. Meng, Y. Zhu and K. L. Liu, *J. Power Sources*, 2022, **545**, 231944.
82 M. J. Shi, B. Wang, C. Chen, J. W. Lang, C. Yan and X. B. Yan, *J. Mater. Chem. A*, 2020, **8**, 24635.
83 X. D. Zhu, Z. Y. Cao, W. J. Wang, H. J. Li, J. C. Dong, S. P. Gao, D. X. Xu, L. Li, J. F. Shen and M. X. Ye, *ACS Nano*, 2021, **15**, 2971–2983.
84 Y. L. Wang, L. W. Liu, Y. P. Wang, J. L. Qu, Y. Chen and J. Song, *ACS Nano*, 2023, **17**, 21761–21770.
85 M. J. Shi, B. Wang, Y. Shen, J. T. Jiang, W. H. Zhu, Y. J. Su, M. Narayanasamy, S. Angaiahc, C. Yan and Q. Peng, *Chem. Eng. J.*, 2020, **399**, 125627.
86 Y. H. Liu, Y. Y. Mei, W. Xu, M. H. Zhang, J. W. Hou and Y. F. Dong, *J. Alloys Compd.*, 2023, **957**, 170397.
87 P. Gao, Z. K. Pan, Q. Ru, J. Zhang, M. H. Zheng, X. Zhao and F. C. C. Ling, *Energy Fuels*, 2022, **36**, 3319–3327.
88 J. Y. Cheng, S. Nan, S. Yu, K. T. Liu, H. G. Gu, L. Tan, Z. L. Niu, D. Li and H. Q. Wang, *Chem. Eng. J.*, 2023, **472**, 144845.
89 J. Lu, H. L. Du, H. Liu, N. Cao, Z. Li and B. Cao, *J. Alloys Compd.*, 2024, **975**, 172934.
90 L. Chen, X. C. Gao, H. R. Nie, Z. Y. Yuan, S. Y. Zhang and H. Chen, *J. Alloys Compd.*, 2023, **958**, 170491.
91 J. Wu, H. H. Liang, J. M. Li, Z. H. Yang and J. B. Cai, *J. Colloid Interface Sci.*, 2024, **654**, 46–55.